UNIVERSITY OF CALIFORNIA

Santa Barbara

A Forward Genetic Study on Neural Tube Development

A dissertation submitted in partial satisfaction of the
requirements for the degree Doctor of Philosophy
in Molecular, Cellular, & Developmental Biology

by

Sarah Abdul-Wajid

Committee in charge:
Professor William C. Smith, Chair
Professor Christopher S. Hayes
Professor Joel H. Rothman
Professor Thomas L. Turner

September 2015

The dissertation of Sarah Abdul-Wajid is approved.

_____

Christopher S. Hayes

_____

Joel H. Rothman

_____

Thomas L. Turner

_____

William C. Smith, Committee Chair

August 2015

ACKNOWLEDGEMENTS

I thank members of the Smith Lab, past and present, for their helpful advice, guidance and participation in my research that culminates this thesis. More importantly, members of the lab supported and encouraged a generous, fun and non-judgmental environment which I truly enjoyed working in everyday. This environment allowed me to succeed and do my best work and for this I owe gratitude to Bill and the Smith Lab.

I also owe thanks to the members of my family who have dealt with my obnoxious attitudes over the course of graduate school. My parents taught me persistence and perseverance, which allowed me to make it through the hardest parts of graduate school. For these character qualities and the opportunity of higher education, I thank them and dedicate this thesis to them.

Eric Turri has been a constant source of love, support and humor during my graduate work and I could have made some /more terrible decisions in my graduate career without his moderating, sarcastic sound board in my life. I thank Eric for this imperative support.

Finally, the 'First Years', have been a critical trifecta of power in my graduate career. I would not have made it past first/every year without them; I would not be the cynical, judgmental scientist I am today without them and I dedicate all of what went down the garborator first year to my best friends for life.

The first chapter of this thesis is a reprint of material published in the May 2014 issue of Genetics. The second chapter is work submitted and in review at Cell Reports as of August 2015.

VITA OF SARAH ABDUL-WAJID

August 2015

EDUCATION

Bachelor of Science in Developmental Biology, University of Toronto, 2007
Doctor of Philosophy in Developmental Biology, University of California, Santa Barbara, September 2015

PROFESSIONAL EMPLOYMENT

Summer 2006: Summer Internship, Xoma Inc. Emeryville, CA
2008-2010: Research Associate II, Department of Immunology, University of California, San Francisco
Fall 2010, 2012, 2013: Teaching Assistant, Department of MCD Biology University of California, Santa Barbara

PUBLICATIONS

Abdul-Wajid S, Morales-Diaz H, Khairallah S, Smith WC. "T-type calcium channels are required for neural tube closure and EphrinA/EPHA expression." *Manuscript in review at Cell Reports, April 2015*
Kourakis MJ, Reeves W, Newman-Smith E, Maury B, **Abdul-Wajid S**, Smith WC. "A one-dimensional model of PCP signaling: Polarized cell behavior in the notochord of the ascidian Ciona." *Developmental Biology. 2014 Nov* 1; 395(1): 120-30
Abdul-Wajid S, Veeman MT, Chiba S, Turner TL, Smith WC. "Exploiting the Extraordinary Genetic Polymorphism of *Ciona* for Developmental Genetics with Whole Genome Sequencing." *Genetics. 2014 May* 197:49-59
Thomas MF, **Abdul-Wajid S**, Panduro M, Babiarz JE, Rajaram M, Woodruff P, Lanier LL, Heissmeyer V, Ansel KM. "Eri1 regulates microRNA homeostasis and mouse natural killer cell development and anti-viral function" *Blood. 2012 Jul* 5; 120(1): 130-42
Vijayanand P, Seumois G, Simpson LJ, **Abdul-Wajid S**, Baumjohann D, Panduro M, Huang X, Interlandi J, Djuretic IM, Brown DR, Sharpe AH, Rao A, Ansel KM. "IL-4 production by Follicular Helper T cells requires the conserved Il4 enhancer HS V/CNS2" *Immunity. 2012 Feb* 24; 36(2): 175-87
Alli Z, Chen Y, **Abdul-Wajid S**, Al-Saud B, Abdelhaleem M. "A role for DHX32 in regulating T-cell apoptosis" *Anticancer Research. 2007 Jan-Feb* 27 (1A): 373-7

FIELDS OF STUDY

Developmental Biology and Genetics

ABSTRACT

A Forward Genetic Study on Neural Tube Development

by

Sarah Abdul-Wajid

My dissertation work has focused on mapping and characterizing a spontaneous neural tube closure mutant, *bugeye*, in the marine, invertebrate chordate organism, *Ciona savignyi*. The work involved developing a new and rapid method of mutation mapping by next-generation DNA sequencing. This new method of mapping was tested on a previously identified *Ciona intestinalis* mutant whose genomic data was used to calibrate mapping parameters and the mapping program for *Ciona* genomes. After successful testing of the mapping program, it was applied to the new *bugeye* mutant in *Ciona*. Mapping revealed a unique and narrow signature of linkage in the *Ciona bugeye* mutant genomes over a predicted T-type calcium channel gene. Requirement for the T-type calcium channel gene in neural tube closure was tested by CRISPR mediated knockout in wild type embryos and definitively established causality of the gene for the *bugeye* mutant phenotype. The *bugeye* mutant was investigated for previously known characteristics of neural tube closure mutants such as neural specification, cellular polarity and apical constriction defects. My results did not support any of these possibilities and rather support the hypothesis that *bugeye* is a failure to maintain a sealed anterior neuropore. To further explore and expand this previously

uncharacterized role for T-type calcium channel genes, I tested for conservation of function in the vertebrate model *Xenopus*. Knockdown of the orthologous and earliest expressed T-type calcium channel gene, CAV3.2, in *Xenopus laevis* embryos via splice-disrupting morpholinos resulted in an open brain phenotype with characteristics similar to that of the *bugeye* mutants – a failure to seal the anterior neuropore. The function of T-type calcium channels in neural tube closure was tested in both *Xenopus* and *Ciona*: cellular calcium fluctuations, using the genetically encoded calcium indicator, GCaMP3, were investigated in the context of neurulation and T-type calcium channel disruption. I also investigated a downstream target of T-type calcium channels and a previously known neural tube closure gene family, the EphrinA family of ligand-receptor signaling molecules. My results found that the *bugeye* mutant phenotype, open brain, could be rescued by down regulation of EphrinA signaling in the neural tube. The cumulative results allowed us to propose a model of T-type calcium channel function in neural tube closure via EphrinA signaling and suggest future directions to further explore this newly established role for T-type calcium channels in sealing the anterior neuropore.

TABLE OF CONTENTS

I. INTRODUCTION

The subject of my dissertation is the genetic control of neurulation. Neurulation is the critical process during development of chordate embryos in which the brain and spinal cord form a closed tube from a sheet of cells known as the neural plate. Disruptions to neurulation can result in severe defects within the brain or spinal cord, often leaving them exposed to the external environment –known as 'open brain' or 'open spinal cord' phenotypes. The starting point for my dissertation work was a forward genetic screen for early developmental mutants in the marine invertebrate chordate *Ciona savignyi*. One line – subsequently called *bugeye* – was identified due to its protruding photoreceptors and brain. The study of this mutant, from mapping the underlying genetic lesion to understanding the role played by the *bugeye* gene in neurulation, forms the basis of my dissertation work. As will be detailed in this dissertation, the *bugeye* mutation led to the discovery of a novel regulatory mechanism in chordate neurulation.

The first chapter of my dissertation describes a new, next generation sequencing-based mutation mapping procedure that I developed for *Ciona* and used to map the *bugeye* mutation. In the second chapter I describe my studies that explored the function of the *bugeye* gene in neurulation in both *Ciona* and a vertebrate model *Xenopus*.

Mapping

For the first chapter of my dissertation, I describe the mutation-mapping program I developed for *Ciona* and, its application first to a previously mapped *Ciona* mutant, as a proof-of-principle, and then to the unknown *bugeye* mutant. Before the development of my mapping program, our mapping methods in *Ciona* were labor intensive and inefficient. While

Ciona has many features that lend themselves to forward genetics, such as its large brood sizes and hermaphroditic nature, the tools for forward genetics were never developed to the extent they are in more common model organisms like *Drosophila* or *C. elegans* (Blumenstiel et al., 2009; O'Rourke et al., 2011). One of the biggest differences with *Ciona* is the absence of established inbred lines. In fact, efforts to make inbred/isogenic lines of *Ciona* have not been successful and instead we maintain our mutant lines by outcrossing to wild-caught animals and then rescreening for the presence of the mutation each generation (Veeman et al., 2011b). Moreover, the genomes of wild isolates of *Ciona* are among the most polymorphic in the metazoans (Leffler et al., 2012). Thus the genetic lesions of mutants are buried in an uncharted forest of inherent genetic variations such as SNPs, INDELs and inversions. In contrast, for inbred genetic model organisms there are databases with extensive documentation of known variations, such as SNPS and INDELs. This reference resource of genetic markers is then used to map and isolate the new genetic lesions of their mutants (Berger et al., 2001; Davis et al., 2005). Without this resource for *Ciona*, I had to develop a novel mapping strategy. While the existing programs searched for the causal genetic mutation by mapping or aligning genetic variants to the databases of known SNPs, the program I developed takes advantage of the high genetic polymorphism of *Ciona* to instead search for areas of isogenicity (lack of variation and polymorphisms or homozygosity) in the genomes of animals homozygous for the mutation. This area of isogenicity is expected as a consequence of the process of genetic linkage on a genetic locus under strong selection (i.e. me, the researcher, selecting out the recessive *bugeye* phenotype) (Watterson, 1978). Identifying a unique region of isogenicity in *Ciona* was plausible due to the preservation of the highly polymorphic background, whereas in inbred organisms large non-unique islands of

isogenicity exist because of continuous selection for lack of variation. In Chapter 1 of my dissertation I describe in detail how I computed isogenicity in the genomes of mutants and wild type embryos for the purpose of mapping.

Recently, the established genetic model organisms also began using next-generation DNA sequencing as means to identify the genetic variants for mutation mapping purposes. Next-generation DNA read sequencing produces millions of short read sequences from a DNA sample, which can then be aligned to create a complete genome sequence. This improved the efficiency of mapping mutations by allowing the experimenter to achieve an entire snapshot of all the variant alleles in an entire mutant genome in one cheap, experimental run. The person-years required to map a mutant went from 5+ to less than 2 weeks (Darby and Hall, 2008; Leshchiner et al., 2012; Schneeberger et al., 2009). Before I joined the Smith lab, *Ciona* mapping methods used bulk segregant analysis of small (<1kb) genomic PCR products to assess SNPs and their linkage (Hackley et al., 2013; Veeman et al., 2011b). This required making PCR products spanning the entire ~160Mb genome, sending these products off for standard Sanger sequencing, and then assessing the linkage of a SNP in each disparate sequencing reaction. Measuring the height of a SNP peak in the mutant sequence and comparing it to the same peak in the wild-type sibling sequence determined linkage (Veeman et al., 2011). Thus my first project was to improve mutation-mapping procedures for *Ciona* by using next-generation sequencing data from both the mutant and wild type embryos. This genomic read data from pools of mutant or wild type genomes allowed me to look at almost every possible variant site in the genome simultaneously (as opposed to piece by piece by PCR). This was beneficial for two main reasons: the number of variant sites influenced the confidence with which I could call a region isogenic, as well as

the size of the isogenic region. One of the shortcomings of the previous mapping method in *Ciona* is the smallest mapping interval that could be reasonably derived often contained hundreds to thousands of kilo-bases, and dozens of gene candidates. Having the ability to look at all variant sites at once, across the entire genome, allowed me to resolve the genetic linkage assessment to finer intervals and thus improved the accuracy of pinpointing the genetic mutation, as it did for other model organisms. Chapter 1 of my dissertation further details the benefits of using next-generation DNA read sequencing from *Ciona* for mapping and again highlights how the highly polymorphic background of *Ciona* actually make them an ideal subject for mapping by next-generation sequencing. The chapter concludes with the successful application of the mapping method on the mutant *bugeye* and effectively decreasing the time required to map a mutant in *Ciona* to ~1 week.

Neurulation

After successful mapping of *bugeye* the second chapter of my dissertation explores the role of the mapped gene, a T-type calcium channel, in neurulation. One of the striking features of *Ciona* larvae is the neural tube, and in particular its close resemblance to the vertebrate neural tube. *Ciona* undergoes primary neurulation similar to vertebrates in which embryonic neural plate thickens, elongates, and then rolls up into the neural tube. This process of primary neurulation involves a precise sequence of collective and cell-autonomous behaviors. Convergent extension and cell intercalation are two behaviors required during neurulation in which cells of the neural plate converge to the midline and then intercalate, resulting in an elongation of the plate in the anterior-posterior axis (Davidson and Keller, 1999). This movement also narrows the neural plate and thickens the cells. Cells at the

midline of the narrowing neural plate display an apically polarized actin-based constriction forcing them into a wedge shape, which results in the formation of the neural folds. Proteins of the actin cytoskeleton, and its regulators like Shroom, APKC and Pars, and microtubules have been shown to be required for cell morphology changes in the neural tube (Eom et al., 2011; Hildebrand, 2005). These wedge cells become the medial neural hinge point of the neural tube and initiate the rounding of the ventral side of the neural tube. Elevation of the neural folds begins on either side of the hinge point and is thought to be dependent on the underlying mesenchyme and on changes of the extracellular matrix surrounding the neural folds (Zohn and Sarkar, 2012). Once the neural folds have elevated the dorsal edges come together at the dorsal surface, contact and fuse. This contact and fusion is mediated by various cell-cell interacting and cell adhesion proteins like Cadherins, CAMS, and Ephrins (Holmberg et al., 2000; Pyrgaki et al., 2011). At the same time as the neural folds contact and fuse, neighboring epidermal cells must extend over and cover the fused, dorsal neural tube. This is driven by epidermal-neural cell-junction remodeling and cell movement (Hashimoto et al., 2015). Once the epidermis covers the fused neural tube, neurulation is complete and further differentiation and specification of the neural tube and neurogenesis proceeds. As mentioned earlier, disruption of many of the genes required for the various steps of neurulation can result in a severe open brain or open spinal cord phenotype. Thus, my first step in the goal of characterizing the T-type calcium channel's role in neurulation was to determine when and where it's function was necessary in the steps of neurulation. After investigating all the hallmarks of neurulation, cell polarity, constriction, and neural differentiation, I identified a role for T-type calcium channel genes in the neural fold fusion step, and linked a known neural fold fusion mediator, the EphrinA family, as a downstream

effector of T-type calcium channel function. Furthermore, I establish functional conservation of this gene in the vertebrate *Xenopus*, and show parallel phenotypes and cellular mechanisms with *Ciona.* This was an interesting result because of the implications it had for other vertebrates, and this was the first demonstration of a role for T-type calcium channels in vertebrate neurulation. Chapter two concludes with a proposed model for T-type calcium channel genes in neural fold fusion and suggests future directions of investigation.

In summary, the overall goal of my dissertation work, to study novel genetic controllers of neurulation, was achieved by developing a rapid and efficient mutation mapping method in *Ciona* and applying it to the open brain *Ciona* mutant *bugeye* and then further characterizing the role of the mutated gene in neurulation in both *Ciona* and *Xenopus*.

II. Mutation mapping in *Ciona*

A. Abstract

Studies in tunicates such as *Ciona* have revealed new insights into the evolutionary origins of chordate development. *Ciona* populations are characterized by high levels of natural genetic variation, between 1-5%. This variation has provided abundant material for forward genetic studies. In the current study, we make use of deep sequencing and homozygosity mapping to map spontaneous mutations in outbred populations. With this method we have mapped two spontaneous developmental mutants. In *Ciona intestinalis* we mapped a short-tail mutation with strong phenotypic similarity to a previously identified mutant in the related species *Ciona savignyi*. Our bioinformatic approach mapped the mutation to a narrow interval containing a single mutated gene, *a-laminin3,4,5*, which is the gene previously implicated in *C. savignyi.* In addition, we mapped a novel genetic mutation disrupting neural tube closure in *C. savignyi* to a T-type Ca^{2+} channel gene. The high efficiency and unprecedented mapping resolution of our study is a powerful advantage for developmental genetics in *Ciona*, and may find application in other outbred species.

B. Introduction

A valuable attribute of many model organisms is the ability to conduct forward and reverse genetics. The availability of sequenced genomes and transcriptomes have streamlined reverse genetic approaches, but forward genetic approaches remain time consuming and cumbersome. Even for organisms with well-developed mutation mapping strategies and resources, classical linkage analysis can be slow and subject to chance. Genome-wide association studies now provide an alternative approach, but are severely limited by the need for high-frequency alleles and very large samples (Cheng et al., 2010;

Marchini et al., 2007). A need remains for additional phenotype-to-genotype strategies in, for example, the investigation of quantitative traits, natural variation, and disease loci (Hillier et al., 2008; Jelier et al., 2011; Lehner, 2013; Liti and Louis, 2012). In recent years, new and inexpensive deep sequencing technologies have created opportunities for forward genetic approaches (Hobert, 2010). By taking a snapshot of variation across the genome of an outbred population a researcher can now quickly identify a region of homozygosity unique to mutant individuals. Variations of this method then use a fine-mapping parameter to define a high-confidence mapping interval, and to retrieve a list of variable sites in the interval as a list of possible causal mutations. Modeling shows that the mapping power using whole genome sequencing (WGS) is a function of how many genomes are sampled from mutant individuals, the recombination rate, and genome coverage (Leshchiner et al., 2012; Obholzer et al., 2012). This approach has worked efficiently and accurately for the well assembled, annotated and inbred genomes of model organisms such as *Drosophila melanogaster*, *Caenorhabditis elegans* and *Mus Musculus* (Andersen et al., 2012; Blumenstiel et al., 2009; Leshchiner et al., 2012).

Tunicates, such as the ascidian *Ciona intestinalis*, are classic model organisms for developmental biology, and as the closest living relatives of the vertebrates they are a key group for understanding chordate development and evolution (Delsuc et al., 2006; Satoh, 1994). As larvae, ascidians exhibit a conserved chordate body plan that includes a notochord and a dorsal hollow central nervous system (Passamaneck and Di Gregorio, 2005). However, the embryos and larvae of ascidians are much simpler than those of vertebrates (e.g., a *C. intestinalis* larva consists of approximately 2,600 cells), and develop according to a fixed cell lineage (Satoh, 1994). Reference genome sequences are now available for both *C. intestinalis*

and the closely related species *C. savignyi*. Both *Ciona* species have compact genomes (~160 Mb) with relatively few protein-encoding genes (~16,000 genes) (Shoguchi et al., 2006; Small et al., 2007b). In addition, both *Ciona* species display very high levels of natural genomic variation; the two haplotypes in the reference genomes of *C. intestinalis* and *C. savignyi* are ~1% and ~4% different, respectively (Dehal et al., 2002; Satou et al., 2012; Small et al., 2007a). Our laboratory has found that a significant fraction of wild-caught individuals from both species carry recessive mutations that can be uncovered by self-fertilization (Veeman et al., 2011a). Because establishing inbred lines of *Ciona* has proven to be very difficult, we maintain mutant and transgenic lines by outbreeding them to wild-caught stocks (Veeman et al., 2011a). Despite this limitation, we have been able to isolate, maintain, and map naturally-occurring mutations in *C. intestinalis* and *C. savignyi* that disrupt processes such as notochord morphogenesis and neural plate development (Hackley et al., 2013; Jiang et al., 2005a; Tresser et al., 2010; Veeman et al., 2008). The high level of genetic variation between individuals has actually aided mapping via bulk segregant analysis by providing an abundance of single nucleotide variation (SNV) markers, although our current mapping procedures are very time consuming.

The WGS mapping method presents a tremendous opportunity to investigate mutations and genetic variation in wild (i.e., outbred) animals. The relatively small size, high recombination rate (~25-200 Kb/cM) (Kano et al., 2006; Small et al., 2007a), and relatively complete reference genomes make the two *Ciona* species ideal models for applying the WGS mapping method for highly polymorphic wild models. Two wild-isolated recessive developmental mutants, one in *C. intestinalis* and one in *C. savignyi*, were used to test the WGS mutation-mapping strategy. We report that via homozygosity mapping we are able to

quickly, and with high resolution, identify mutant loci in both species. The smaller genomes and higher polymorphism rate of the *Ciona* species allowed us to define narrower candidate regions than has been reported for vertebrate models.

C. Methods

Genomic DNA isolation

Larvae were incubating in 0.5M EDTA with gentle pipetting for 30 minutes to remove maternally-derived follicle cells before being homogenized for gDNA isolations as described previously (Silva and Smith, 2008). Upwards of 300 larvae were used for sufficient genomic DNA collection.

Ciona Mutation Mapping strategy

The *C. savignyi* and *C. intestinalis* unmasked reference genomes were downloaded from ftp://ftp.ensembl.org/pub/release-73/fasta/ciona_savignyi/dna/ and http://ghost.zool.kyoto-u.ac.jp/datas/JoinedScaffold.zip, respectively. The Illumina sequencing reads were aligned to their corresponding reference genomes using the Burrows Wheeler Aligner program (version 0.5.9) (Li and Durbin, 2009). Default parameters for the 'bwa aln' command were used for all alignments. Following alignment, Samtools (version 0.1.18) were used to generate pileup files from reads of mapping quality $\geq$ 15, and base quality $\geq$ 15 (Li et al., 2009). The pileup file was used to compute homozygosity for genome-wide mapping using custom scripts in Python and R (Python v2.7 and R-project.org). For the homozygosity calculation, the program first discerned whether a genomic base position was covered by more than 10 reads, if so then it proceeded to count the percentage of aligned bases at that position that matched each other. If 85% or more of the aligned bases at the position were in agreement then that site was considered homozygous. The program summed the amount of

homozygous sites within a designated genomic window size (5 Kb for *C. savignyi* and 10 or 20 Kb for *C. intestinalis)* and divided by the number of informative sites (>10X coverage sites) in that window. This yielded a proportion or percentage of homozygosity for each genomic window across the entire genome. These values were transferred to R and graphically depicted. The peak homozygosity values are also called from the output file and left to the user to visually verify in the R plot.

Once the ROI is identified from the second step, the corresponding pileup file is used for the fine-mapping program. In step 2 of the program, the major allele frequencies for each variant site (with coverage greater than 5 reads) is calculated. The fine-mapping program used only SNV allele frequencies between 40-85%. We used this allele frequency filter to exclude the high amount of population-specific variation in the >85% allele frequency range and the inherently large number of homozygous SNVs as we approached the mutant locus. The <40% filter was used to exclude minor-allele frequencies, potential sequencing errors, and focuses on the major allele of each SNV. These 40-85% allele frequencies were binned in 100 bp windows and listed in the output file, which is used for plotting in R. The program outputs the position of the largest stretch of windows with zero heterozygosity and the user can verify if the bin output is unique to the ROI, within a trough trending to zero-values (as this was not the case for the C. *savignyi bug* fine-mapping). All LOESS lines for the *C. savignyi* data were computed in R by calling the LOESS function and using a span of 0.2 (R project, Manuals).

Downstream gene model alignment was carried out using the Integrative Genomics Viewer software from the Broad Institute (Robinson et al., 2011; Thorvaldsdottir et al., 2013).

qRT-PCR

RNA was extracted from mutant and wild-type larvae using Trizol (Invitrogen) after follicle cells were removed, as above. Two hundred nanograms of total RNA was used for cDNA synthesis using Superscript III First-Strand Synthesis kit (Oligo dT primer, Invitrogen). One microliter of this cDNA reaction was used for each qRT-PCR reaction with Fast Sybr Green 2X MasterMix (ABI). Primers are listed in Supplemental Table 2. Genes used for the first ΔCT normalization calculation were *C. intestinalis* Actin and *C. savignyi* RPS27A (Olinski et al., 2006). Wild-type values were used for the second ΔCT calculation. qRT-PCR reactions were run in triplicate and each experiment consisted of three biological repeats.

D. Results

Ciona Mutant Lines

The bottleneck for large-scale mutation screening and characterization has been the time-consuming process of mapping mutant loci. We asked whether homozygosity mapping via WGS, as used in previous inbred model organisms (Blumenstiel et al., 2009; Leshchiner et al., 2012; Obholzer et al., 2012), would accurately and efficiently allow mutation identification in *Ciona*. To test this, we developed a bioinformatics strategy and applied it to two novel mutant lines, one in *C. intestinalis* and the other in *C. savignyi*. The *C. intestinalis* mutant had a short-tail phenotype (Figure 1A and B) closely resembled the *chongmague* (*chm*) mutation previously isolated from the related species *C. savignyi* (Veeman et al., 2008), and was named *chm-like*. A cross-species fertilization test indicated that the *C. intestinalis* mutant was in the same complementation group as the *C. savignyi chm* mutant (data not shown). In a previous report we showed that the *C. savignyi chm* phenotype is due

to a profound disruption in notochord morphogenesis caused by a null mutation in the *a-laminin3,4,5* gene (Veeman et al., 2008). The second mutant, in *C. savignyi*, was identified in a self-fertilization screen and has the defining characteristic of an open anterior neural plate with a protruding and exposed brain, and was named *bugeye, (bug)* ((Veeman et al., 2011a), Figure 1C and D). Both *Ciona* mutants were scored as phenotypically recessive.

The first step of the strategy consisted of spawning heterozygous parents (+/*m*) to generate F1 progeny (Figure 1E). An adult *Ciona* will typically spawn several hundred eggs (and countless sperm). For mapping of the *C. savignyi* mutant we tested samples of both self-fertilized gametes from a single hermaphroditic parents (SPP samples, Table 1), and of crossed gametes from several +/*m* parents spawned together (MPP samples, Table 1). For the *C. intestinalis* mutant only a crossed-gamete sample was tested. Samples consisted of the pooled genomic DNA from 600 to 800 homozygous mutant (*m/m*) progeny, and for the *C. savignyi* mutant a separate pool +/+ and +/*m* siblings, called the WT sample, was prepared (Table 1). The genomic DNA pools were used to create libraries for 50 cycle/single-end Illumina sequencing. The resulting reads (~150 million) were then used as the input for the next step of the mapping program.

Homozygosity Maps

Construction of genome-wide homozygosity maps was the next step in the program. Loci linked to the causative mutation should be evident by a cluster of windows with higher than average homozygosity – approaching complete homozygosity (i.e., 100% homozygous values). For *bug* we generated both a cross-fertilized dataset, in which twelve heterozygous *bug* adults were spawned together, and a self-fertilized dataset in which all embryos contributing to the genomic DNA pool derived from a single heterozygous *bug* adult (Table

1). For *chm-like* only a single cross-fertilized dataset was generated. For the initial round of mapping we used the two cross-fertilized datasets. Mapping with self versus cross-fertilized datasets will be treated separately, below.

To map the homozygosity, the Illumina sequences were first aligned to their respective reference genomes and filtered for mapping and sequence base quality *(Dehal et al., 2002; Small et al., 2007b)*. Using a cutoff of MapQ greater than or equal to 15 (Table 1, Figure S1), 68% of the *C. intestinalis* reads mapped to the genome, versus ~40% of the *C. savignyi* reads (Table 1). The overall coverage from the *C. savignyi* datasets was highly variable, due to poor mapping quality (Figure S1). The *C. savignyi* reference genome consists of 374 reftigs with an N50 of 1.8 Mb (Small et al., 2007b; Vinson et al., 2005). Two hundred and twenty-seven of the largest reftigs were roughly mapped into 14 linkage groups, corresponding to the 14 chromosomes (Hill et al., 2008). The difficulty in aligning the *C. savignyi* reads to the reference genome is primarily a reflection of the highly polymorphic nature of the wild *C. savignyi* population, with an estimated ~3-5% genome-wide variation between haplotype isolates (Small et al., 2007a). Thus a lower percentage of the *C. savignyi* reads were aligned to the reference genome; there were more mismatches per 50bp read in this species, and thus more alignment penalties and lower mapping quality (Supplemental Figure 1 and 2). This biased coverage in *C. savignyi* to areas of lower heterozygosity, such as exons (Supplemental Table 1). Nevertheless, we were able to obtain 13 to 22 X coverage of the *C. savignyi* reference genome with the MapQ≥15 reads, for the four datasets. The difference in the mapping quality of the two species resulting from the higher variation of *C. savignyi* can be seen in comparisons of the edit distances (i.e., the minimum number of changes required to transform one sequence into the other) of two randomly chosen sets of 5

million reads the two genomes (Figure S2). Thus many reads fail to map to the reference genome due to natural variations causing multiple mismatches that exceed the cutoff. The higher sequence variation of *C. savignyi* also likely resulted in a high fraction of reads scoring as "repeated", versus those from *C. intestinalis* (Figure S2). We did not investigate whether reducing the mapping stringency could lead to a higher percentage of the reads mapping, as this also has the potential to result in reads being incorrectly mapped on the genome. Moreover, as we will describe below, we were able to successfully map the *C. savignyi* mutation despite the low percentage of reads that mapped.

The post-alignment, quality-filtered, sequence reads were used for mapping analysis. A relative homozygosity value was calculated for non-overlapping windows of 5 Kb for *C. savignyi*, and 10 Kb for *C. intestinalis* datasets. Homozygosity is calculated by determining the percentage of base positions, within the windows, in which ≥85% of the sequence reads at each position, are in agreement. This calculation simplifies the analysis and reduces computing time by focusing on regions with high homozygosity. With expected sequencing error rate of ≈1-5%, we would not expect estimates of homozygosity to reach 100% for all sites within any window (Luo et al., 2012). We set our homozygosity cutoff well below this error rate (i.e., 85%). Therefore a 100% homozygosity window in our analysis would be defined as one in which all 5,000 or 10,000 base positions are at least 85% in agreement. Other cut off values were tested, and values greater than 85% yielded minor differences in window values, but did not change the identity of the windows with peak homozygosity. Within each window, we only considered bases with ≥10-fold read coverage. The relative homozygosity measure also adjusted for areas of variable coverage by adjusting window sizes to the number of useable sites in a window (e.g., if only 9,680 bases out of 10,000 in a

window had coverage greater than 10, then homozygosity was calculated as a percentage of the 9,680 bases in that window). On average, the *C. savignyi* datasets had ~74% useable sites per window. In contrast, the *C. intestinalis* dataset yielded an average of 95% useable sites per window (Table 1). Because of the lower overall coverage for *C. savignyi*, we added a minimal requirement that at least 40% of the bases within a window have ≥10-fold coverage to be used in the analysis.

For the *C. intestinalis* dataset, the average homozygosity of all windows was 98.3% (i.e., 1.7% variable); while for the *C. savignyi* datasets the average homozygosity was ~96.7% (i.e., ~3.3% genomic variability, Table 1). These values are in agreement with previous estimates of genomic variation in *C. intestinalis* and *C. savignyi (Satou et al., 2012; Small et al., 2007a)*. When the distribution of percent homozygosity values across the genome for the *C. intestinalis chm-like* was examined, it was apparent that chromosome 2 contained a uniquely homozygous region with a single peak (100% value) at 2.76 Mb (red arrow, Figure 2A).

For the *C. savignyi* dataset, a simple plot of percent homozygosity versus the assembled linkage groups (LG) produced a noisier plot than for *C. intestinalis*, in which the peak homozygosity was less apparent (upper plot, Figure 2B). Complicating the situation, a large number of small reftigs in the *C. savignyi* reference genome have not mapped to linkage groups (Hill et al., 2008). These are shown clustered at the right end of the plot. In order to better identify the genomic region of peak sequence homozygosity in the homozygous mutant genomes we subtracted the percent homozygosity values of the WT sample from the m/m sample to generate Δhomozygosity values. The subtraction potentially controls for the

variation in homozygosity across the genome of natural populations introduced by mutation rate variation, genetic drift, and natural selection.

From the "subtracted" plot in Figure 2B a region of interest (ROI) can readily be identified on linkage group 11, with reftigs 46 and 77 showing high homozygosity values. We also observed the high homozygosity values for several of the unmapped reftigs, which are shown grouped together at the right side of the plot (Reftigs 183, 532 and 616). The highest cluster of genome-wide Δhomozygosity values centered around the 60 Kb position of reftig 183. These highly homozygous reftigs correspond to highly linked loci, and consequently we can roughly place the unmapped contigs in the vicinity of linkage group 11. Because most of the reftigs had been mapped using only single markers for linkage analysis, their relative orientations are not known (Hill et al., 2008). Contiguity of the roughly mapped reftigs remains largely unknown, unlike in *C. intestinalis* whose physical map was made by a combination of BAC and FISH data (Shoguchi et al., 2006). The quantitative linkage data provided by the *C. savignyi* datasets allowed us to estimate the relative positions of previously unmapped reftigs 183, 616 and 532 relative to reftigs 46 and 77. A large gene model is split between the 3'-end of reftig 532 and the 3'-end of reftig 183, indicating that reftig 532 sequence is continuous with and in reverse orientation relative to reftig 183. There are also large gaps (stretches of Ns) near the high homozygosity values found on reftig 616 and 183. Our discontinuous high homozygosity values on each of these reftigs, near large gaps, may indicate misassembly at these specific reftig locations. Our results suggest that reftigs 183, 532 and 616 likely belong on linkage group 11 between reftig 77 and 46. Several other potentially linked (but unmapped) reftigs having slightly lower homozygosity values

(e.g., reftig 370, 494 and 556, Figure 2B) and likely belong on linkage group 11, but no placement or orientation information could be confidently inferred from our linkage analysis.

The incomplete nature of the *C. savignyi* reference genome and the poor mapping of the reads (supplemental table 1, supplemental figure 2), resulted in multiple reftig peaks, and interspersed coverage within the reftigs, so we analyzed the distribution of Δhomozygosity values with 1Kb intervals for each of the individual candidate reftigs separately (Figure S4A). Overall, reftig 183 had the highest cluster of Δhomozygosity values and the highest median (max = Δ 4.8%, median = Δ 3.46%, Figure S4A). Based on these data we chose the 340 Kb reftig 183 as our ROI.

To assess the utility of calculating Δhomozygosity values, we examined the genome-wide homozygosity using only the *m/m* dataset (i.e., without subtraction of WT dataset homozygosity values). Although the plot was much noisier, reftig 183 could still be discerned as having the highest homozygosity values (Figure 2B and Supplemental Figure 4). The five highest values of homozygosity in the *m/m* dataset were found on reftig 183 (3 values), reftig 117 (1 value) and reftig 209 (1 value). Reftigs 117 and 209 were also found to have the same high homozygosity values in the matching wild-type data. In the *m/m* only plot, linkage group 11 also had a unique clustering of windows with high homozygosity values, although it was much less apparent (compare subtracted versus unsubtracted plots, Figure 2B). For the *m/m*-only analysis, the peak of homozygosity on reftig 183 was calculated to be at ~217 Kb, while for the Δhomozygosity analysis, the peak on reftig 183 was determined to be at ~57 Kb (Figure 4A). These results demonstrated that the wild-type dataset eliminated many of the unlinked, inherently high homozygosity values found in the *C. savignyi* dataset.

Having identified ROIs for both the *chm-like* and *bug* mutants we proceeded to higher resolution mapping to identify the causative mutations for the two lines. Because of inherent differences in the degree of polymorphism of the two genomes, and differences in reference genome quality, we found we had to use different fine-mapping approaches for the two mutants, and thus they are treated separately, below.

Fine mapping C. intestinalis chm-like

For fine mapping of *chm-like*, a 1 Mb ROI centered on the peak of the genome-wide map (chromosome 2:2.4-3.4 Mb) was used (Figure 3A). Unlike for genome-wide mapping, in which only the proportion of invariable sites was used to measure homozygosity [equivalent to Watterson's theta (Watterson, 1975)], for fine mapping in *C. intestinalis* we computed the frequency of the major allele at each SNV, using only SNVs covered by 5 or more reads. One hundred base-pair bins of the average major allele frequencies were then calculated across the ROI. We lowered the fold-coverage threshold in this analysis in order to exclude fewer base positions in the interval and achieve the most complete picture of linkage. By definition, the ROI is characterized by the presence of high frequency alleles, and for fine mapping we want to visualize the disappearance of lower frequency alleles as we approach the causative mutation. Our analysis only included bins where the non-reference allele frequency was in the 40-85% range, thereby excluding both the lowest (and possibly erroneous) allele frequencies, and the highest (possibly completely homozygous) alleles. These bins were plotted against genomic position in the ROI. A distinct trough ~100 Kb in heterozygosity is seen centered around position 2.73 Mb and was defined as the mapping interval (MI; Figure 3A). The trough contained five predicted genes, including *a-*

laminin3,4,5, which was located in the longest segment with zero heterozygosity (star, Figure 3A).

Although the window of peak homozygosity (Figure 2A) did not include the a-*laminin3,4,5* gene (it was located 2 windows away), we found that if the window size of genome-wide homozygosity analysis was changed from 10 to 20 Kb, the peak homozygosity window landed directly on top of the *a-laminin3,4,5* gene (Figure S3). Increasing the window size appeared to eliminate minor differences in the number of measurable sites between windows (e.g., a 100% homozygous window only compromising 9,984 measurable sites versus a window with 9,999 homozygous sites out of 10,000 measurable sites).

Examination of the aligned read sequences from the homozygous mutants identified a nonsense mutation in the third exon of α-*laminin3,4,5* gene at position 2,734,938 of Chr2 (Figure 3B). This mutation was found in all 36 reads that covered this position. As this nonsense mutation lies at the beginning of the protein coding-region of the gene, it would almost certainly create a null allele. In addition, the *α-laminin3,4,5* transcript of the *C. intestinalis* mutant was reduced 5-fold, as measured by qRT-PCR (Figure 3C). A similar reduction in transcript level has been seen for other *Ciona* mutant genes, including in *C. savignyi chm (Veeman et al., 2008)*. Based on the similar phenotype, complementation results, and nature of the mutation we concluded that this short-tail mutation is a *C. intestinalis* ortholog of the *C. savignyi chm* mutation.

Mapping a neural tube closure mutation in C. savignyi

Because of the low and uneven coverage for the *C. savignyi* sample, we found that analyzing windows of average allele frequency, as was done above for the *C. intestinalis chm* mutation, yielded inconclusive results, with several regions showing apparent drops in

heterozygosity (Figure S2, and data not shown). As an alternative approach, we tested homozygosity mapping with smaller windows in the ROI. In addition to calculating homozygosity, we computed a local polynomial regression line of best fit (LOESS) based on the available homozygosity values of the ROI and to make the best estimate of peak homozygosity given incomplete coverage and information (Figure 4A). In the LOESS curve a gradual increase in homozygosity is seen in the 50-90 Kb region of the ROI, with a corresponding peak over a predicted T-type calcium channel gene [*CAV3* (Okamura et al., 2005a); Figure 4A]. qRT-PCR analysis revealed that the expression of *CAV3* is reduced ~25-fold in *bug/bug* embryos relative WT embryos (Figure 4B). None of the genes flanking CAV3 in the ROI appeared to be strong candidates for the *bug* mutation. Neighboring genes included a *cation-independent mannose receptor* (*MR*) and a *fibronection leucine rich transmembrane receptor 2* (*FLRT2*). Only synonymous changes were found in the mutant *FLRT2* sequence and a few non-synonymous changes in the mutant *MR* sequence (data not shown). Moreover, the expression level of these genes was similar between mutant and wild-type animals (Figure 4B). Other genes in the ROI, a *phospholipid scramblase,* a ribosomal protein, and *Ras-related Rab21* (Figure 4B) were excluded as *bug* candidate loci based on the ubiquitous nature of their gene function and lack of non-synonymous changes. The sequence for *CAV3* from the homozygous *bug* mutants revealed a number of nucleotide changes resulting in non-conservative amino acid substitutions (Table 2). In addition to the amino acid substitutions, we identified an 81-bp insertion upstream from the predicted start methionine, in the putative *cis*-regulatory region. This insertion was bound at each end by a direct repeat of a 10-bp element found as a single copy in the WT assembly (Figure 4C). This 10-bp element was repeated an additional three times within the insertion. This

insertion has the characteristics of a footprint from an excised transposable element (Kawakami et al., 2004; Scott et al., 1996). This insertion in the putative *cis*-regulatory region may account for the reduced expression of *CAV3* observed in the mutant.

Given the mapping predictions for *bug* and the reduced expression of the *CAV3* allele in *bug*, we hypothesize that disruption of *CAV3* underlies the *bug* phenotype, and the large insertion in the putative *CAV3* promoter to be the likely causal mutation.

Self versus cross-fertilization mapping

To further demonstrate the utility of the mapping strategy with wild isolated mutants in *Ciona*, we also sequenced the self-fertilized progeny (homozygous mutant and WT progeny, ~600 each) from a single heterozygous *bug* adult. We used a gravid adult, heterozygous for *bug*, different from those used in the above analysis, and spawned it multiple times to collect enough progeny for sequencing. The mean genome-wide homozygosity values for both mutant and WT samples were 96.7% (only 0.2% higher than cross-fertilized *bugeye* dataset, Table 1). The genome-wide homozygosity mapping from the single parent identified the same reftig peaks as were found in the dataset from multiple parents (Figure 5). Although the Δhomozygosity values were slightly lower for the self-dataset, the overall noise was reduced. The ROI, reftig 183, and the predicted genetic mutation in the two datasets were also found to be similar. These results demonstrate the feasibility of mapping directly from the mutant progeny of a single wild *C. savignyi* founder adult, which will considerably accelerate the screening and mapping of mutants.

E. Discussion

Our results demonstrate the successful application of a whole-genome mapping strategy in two outbred *Ciona* mutant lines. WGS mutation mapping strategies have been reported

for several genomically well-defined models organisms, including *Drosophila melanogaster*, *Caenorhabditis elegans*, *Danio rerio*, and *Mus musculus*(Blumenstiel et al., 2009; Leshchiner et al., 2012; Obholzer et al., 2012). The theoretical linkage analysis behind published WGS mapping methods and our method is very much the same. The differences lie in how each method computes linkage for the different genomic backgrounds and subtleties of each model organism. Published methods have made use of databases of SNP markers and reference or parental genetic background information in computing homozygosity (Doitsidou et al., 2010; Miller et al., 2013). By contrast, our homozygosity analysis makes no assumption and uses no information about parental or background genetic markers. Our unique approach simply asks for the greatest preservation of homozygous sequence (as opposed to individual SNP markers) as determined by the aligned and variable genomic sequencing reads. This works for *Ciona* and should work for other highly polymorphic/wild genomes where both genetic marker information may be unavailable and polymorphisms disrupt sequence homogeneity frequently. This approach may not be as effective for inbred genomes, which by nature contain large intervals of high homozygosity, or for species that are inherently highly homozygous. However given a highly polymorphic genome, our approach simplifies the computation for homozygosity analysis by only calculating a simple binary problem across the whole genome and not deriving allele frequencies for millions of SNPs. Unlike the results of other methods, this simple computation may be sufficient to identify the candidate gene in genomes like *Ciona* as revealed by our narrow and extremely close peak calls at the whole-genome scale. Previous methods supplemented homozygosity analysis with fine scale allele frequency mapping and still yielded, at best, 800 Kb mapping intervals (Leshchiner et al., 2012).

Ciona presents a unique system for identifying spontaneous mutants. In temperate regions of the world *Ciona* species are present in enormous numbers in places such as harbors, where they are considered a nuisance. The facts that both *C. savignyi* and *C. intestinalis* are hermaphrodites with a capacity to self-fertilize, and that the wild population of both species harbor lethal recessive mutations at high frequency, make them ideal models (Veeman et al., 2011a). The WGS mapping strategy presented here will greatly accelerate gene discovery in *Ciona*. The two species used, *C. intestinalis* and *C. savignyi*, differ significantly in their natural levels of heterozygosity (Dehal et al., 2002; Small et al., 2007a), which necessitated different approaches for fine mapping. The more polymorphic species, *C. savignyi*, presented several challenges due to its high sequence variation. The *C. savignyi* data set was generated from the progeny of twelve heterozygous parents, giving the potential for high genetic variation at all loci. This was evident in the lower percentage of sequence reads mapping to the reference genome when compared to *C. intestinalis*. Relaxing the stringency of read mapping might allow sequences with a greater degree of variation from the reference genome to be successfully aligned, but this will also increase mis-alignment and add noise. Mapping using longer reads or only transcriptome or coding regions might be another feasible approach for *C. savignyi* (Hill et al., 2013).

The *C. intestinalis chm-like* mutation proved to be an ideal test for the WGS strategy. The similar phenotype and complementation data meant that we were starting with a strong candidate. Although we strongly suspected that the *C. intestinalis chm-like* mutation would map to *a-laminin3,4,5*, the availability of orthologous mutations in the two *Ciona* species will provide a valuable research tool. Previous studies of the *C. savignyi chm* mutation show that a loss-of-function allele severely disrupts convergent extension in the notochord

(Veeman et al., 2008). Our initial genome-wide homozygosity mapping with 10 Kb windows identified a peak-homozygosity window 25 Kb from the causative mutation. In retrospective analysis, we found homozygosity mapping with 20 Kb windows would have mapped peak homozygosity directly on the *a-3,4,5-laminin* gene. The mapping of other *C. intestinalis* mutations in the future will indicate whether mutant genes can be identified from plots of homozygosity, without the need for fine mapping, as is now carried out in other species (Leshchiner et al., 2012; Obholzer et al., 2012). We have reason to be confident that the WGS strategy in *Ciona* will consistently give higher resolution mapping than, for example, in zebrafish, in which mapping intervals have been reported to be in the range of 800 Kb (Leshchiner et al., 2012). Modeling with zebrafish data indicated that much smaller mapping intervals could be achieved with greater sampling of individuals (Leshchiner et al., 2012). Because of the relatively small size of the *Ciona* genome compared to the zebrafish genome (160 Mb versus 1.9 Gb), and our large input pools (>400 individuals), we are able to sample many more individuals for an equivalently-sized data set. The highest average coverage we achieved was 34X. However, the sampling from the input pool of individuals within a window is much higher than 34X. For example, a 1 Kb window with 34X coverage would contain an average of 680 50-bp reads. Each of these reads would be randomly derived from the genomes of the input pool. Thus, the ability to detect rare recombination events in genomic regions immediately flanking the causative mutation is very high. The mapping interval we defined for the *C. intestinalis* dataset was approximately 100 Kb. However the causative mutation was found in a 17 Kb interval corresponding to the longest stretch with 100% homozygosity, suggesting that the mapping ability may be much higher, and smaller than the average per-site recombination rate [25-49 Kb/cM (Kano et al., 2006)].

Should the same be found for mutations mapped in the future, this would indicate a mapping precision higher than one centimorgan. Furthermore, the narrowest mapping intervals depend on the availability of informative SNVs across a genome. The more sites in a genomic region, the more potential there is to detect a recombination event. *Ciona*, has the highest known abundance of SNVs of any sequenced animal: In a 10 Kb region, *Ciona* has on average ~170 potential sites useful for detecting rare recombination events that can be used for linkage analysis. By contrast, zebrafish would, on average and depending on the strain, have only 20 of these potentially informative sites within the same window (Guryev et al., 2006). One can imagine how combining this increased site frequency with increased sampling would yield narrow mapping intervals for linkage analysis.

For mapping *C. savignyi bug* we included a WT dataset that would potentially control for unlinked variation in homozygosity. Subtracting the WT homozygosity values reduced the noise and appears to have allowed us to map closer to the candidate mutated gene in the genome-wide mapping (comparing the 217 Kb peak prediction of *m/m* only with the 57 Kb peak prediction of *m/m* - WT on reftig 183; Figure 3D). Additionally, the fact that a large number of reftigs remain unmapped in *C. savignyi* gives extra value to the WT dataset in providing confidence that unmapped reftigs are truly linked. Moreover the WT sample contained the progeny from 12 outbred parents, and thus may provide a reference for population-wide genomic regions of low heterozygosity that can be used with future *C. savignyi m/m* datasets.

The *bug* mutation severely disrupts anterior neural tube closure. There are several lines of evidence supporting CAV3 as being the causative gene for the *bug* mutation. Aside from the genetic linkage, the transcript of this gene is down-regulated 25-fold. We have

previously shown that depletion of Ca^{2+} during *C. intestinalis* neurulation causes profound defects to anterior neural tube development, including an open neural plate phenotype in ≈40% of embryos, which is consistent with our findings here for CAV3 (Hackley et al., 2013). Although known to have early embryonic expression in the developing vertebrate anterior neural tube (Lewis et al., 2009; Perez-Reyes, 2003), to our knowledge this is the first implication of a T-type calcium channel's involvement in neurulation and potentially neural tube closure. One of the advantages of *Ciona* compared to their vertebrate cousins is their lower genetic redundancy. The *Ciona* genomes appear to encode a single T-type Ca^{2+} channel (Cav3), which is the ortholog of the vertebrate *Cav3.1*, *Cav3.2* and *Cav3.3* genes (Okamura et al., 2005a). Further characterization of CAV3 expression and the *bug* mutant will reveal new insights into how Ca^{2+} channels may contribute to the proper development of chordate CNS. A full description of the phenotype, and its causative link to CAV3 disruption, will follow in a separate publication.

Thus the small genome size, high heterozygosity (i.e., high density of genetic markers), and fecundity of *Ciona* all favor the whole-genome approach to mutation mapping. Finally, we show that it is possible to map a mutation using self-fertilized progeny from a single founder animal. Taken together, this mapping strategy removes the single largest bottleneck in the characterization of spontaneous mutants in these key chordate organisms

F. Figures and Figure Legends

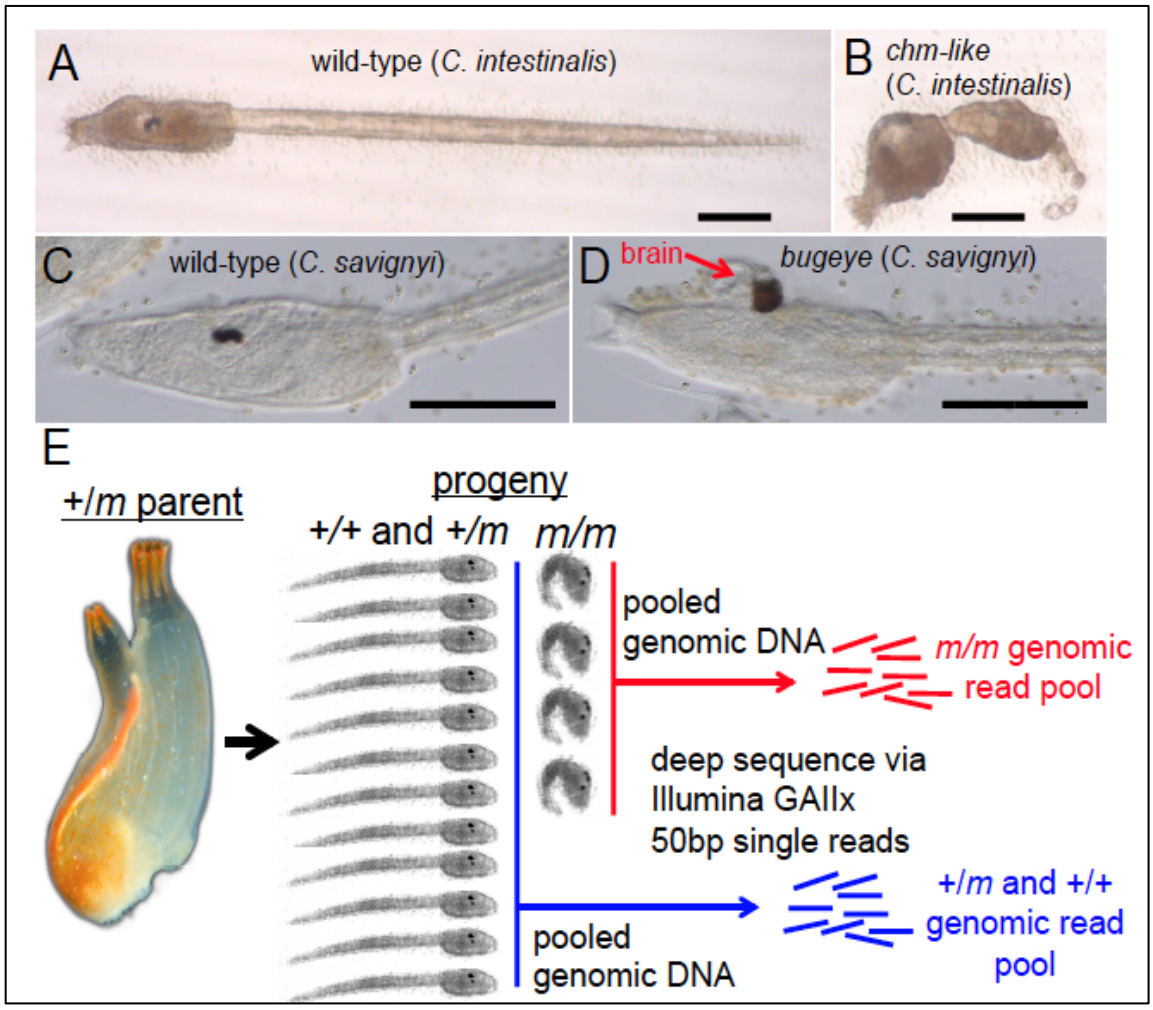

Figure 1. *Ciona* Mutation Mapping **A)** Wild-type *C. intestinalis* larvae. **B)** *C. intestinalis* larvae homozygous for the *chongmague-like* (*chm-like*) mutation. **C)** Wild-type *C. savignyi* larvae. **D)** *C. savignyi bugeye* (*bug*) mutant. The brain protruding from the *bug* mutant is indicated by a red arrow. **E)** Spawning and self/cross-fertilizing adult *Ciona* heterozygous for the recessive mutant '*m*' allele. DNA was isolated from the hundreds of mutant progeny (*m/m*), and when included, their corresponding wild-type (WT) siblings (+/+ and +/*m*). Bars in A-D indicate ~ 100 mm.

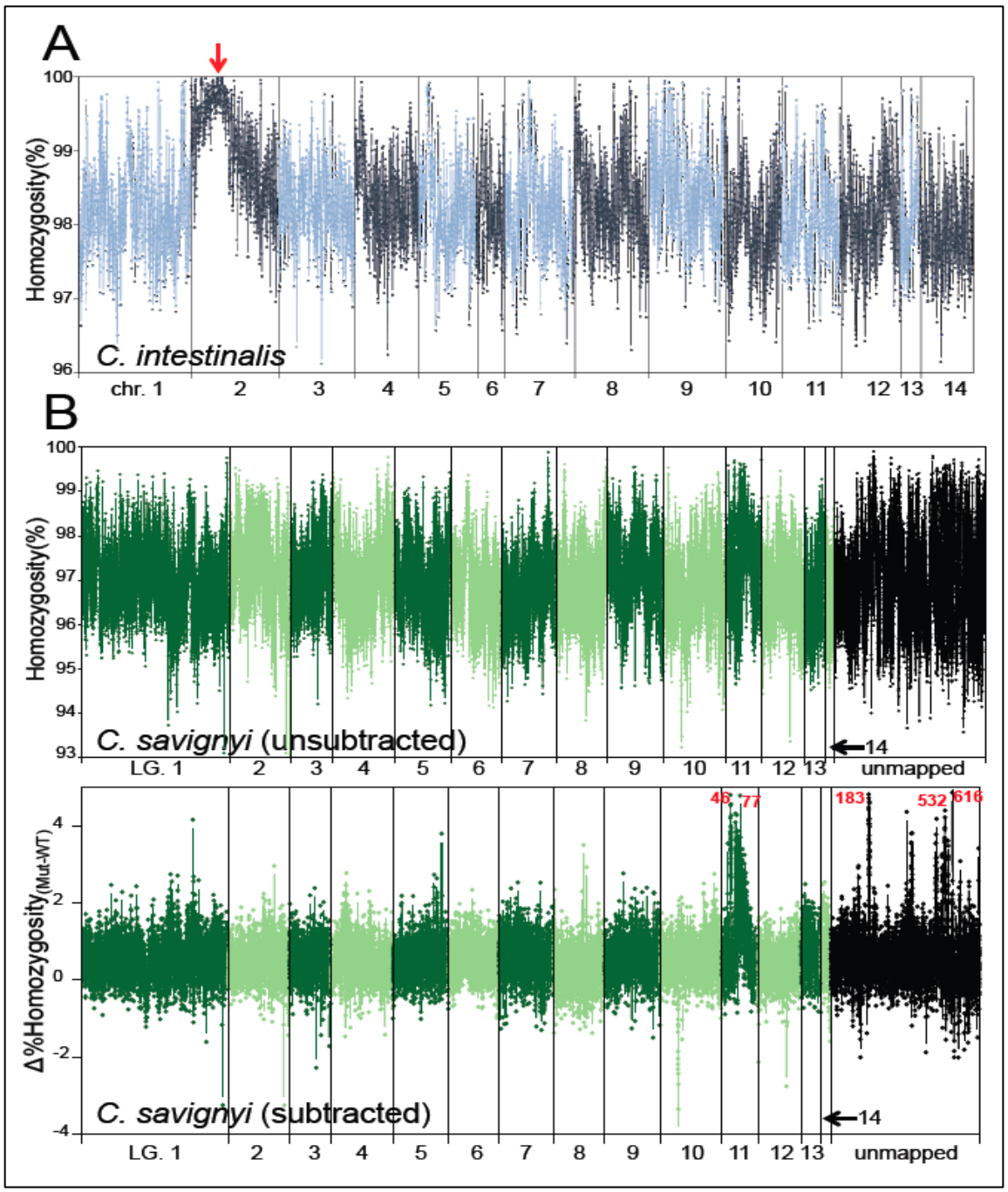

Figure 2. Genome-wide homozygosity maps. **A)** Percentage homozygosity for non-overlapping 10 Kb windows from a pooled sample of embryos homozygous for the *C. intestinalis chm-like* mutation. The highest homozygosity value was at ~2.76 MB in chromosome 2 (red arrow). Chromosomes are depicted in alternating dark and light colored

lines. **B)** Two homozygosity plots are shown for the *C. savignyi bugeye* (*bug*) mutation dataset. The top plot (unsubtracted) shows the percent homozygocity values for 5 Kb windows of aligned sequences reads from homozygous *bug* mutants (m/m) across the fourteen linkage groups, as well as unmapped reftigs. Alternating light and dark lines delineate the linkage groups. Unmapped reftigs are place at the end (black points). In the bottom plot (subtracted) the percent homozyogosity values of aligned genomic reads from the wild-type siblings were first subtracted from the m/m values, generating Δhomozygosity values. In the lower plot, several regions of high relative homozygosity were observed. Reftigs 183, 616, 532, 46 and 77 had the highest values as marked in bold red text. Lower peaks in homozygosity were on reftig 370, 494 and 556. LG= linkage group.

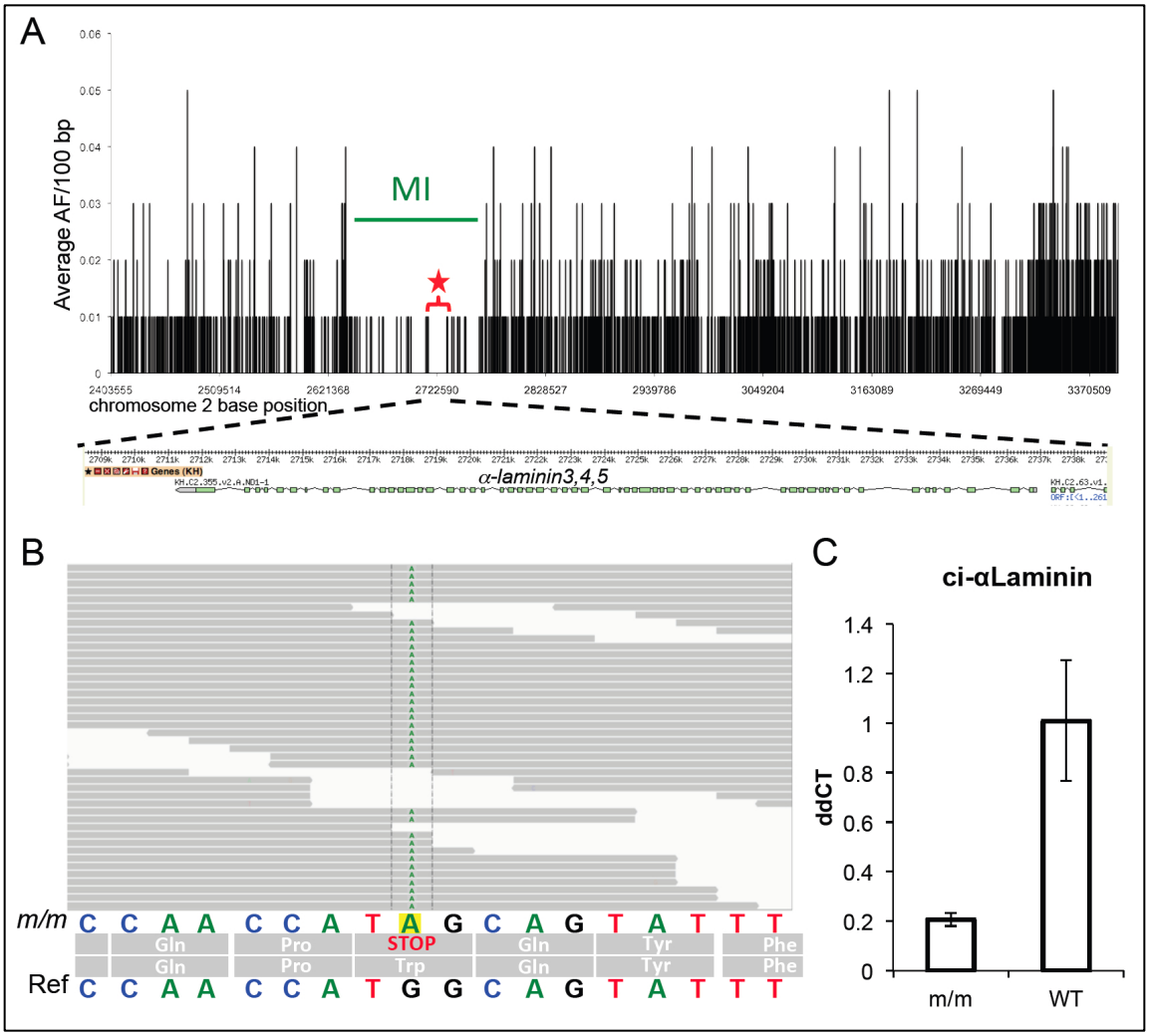

Figure 3. Fine-mapping of the *chm-like* mutation. **A)** The average allele frequency (AF) for 100 bp windows is plotted against nucleotide position for a 1 Mb region of interest (ROI) from chromosome 2 (2.4 Mb - 3.4 Mb). The likely causative mutation was found in a 17 Kb segment from 2.714 to 2.731 Mb. Interestingly, this region was the longest stretch with a complete absence of heterozygous allele frequencies (red star and bracket). A schematic of the a-laminin3,4,5 gene model is shown below the graph. **B)** The nonsense mutation (G to A)in the *a-laminin3,4,5* gene was found in all the of the aligned *m/m* reads. The sequence of the reference genome (ref) is shown at the bottom. **C)** qRT-PCR of *a-laminin3,4,5* in

homozygous mutant (*m/m)* and WT cDNA samples. Bars indicate average of three samples and error bars calculated based on standard deviation in the three replicates. ddCT values were calculated by normalizing to Actin cDNA levels within each sample and then comparing mutant and wild-type levels.

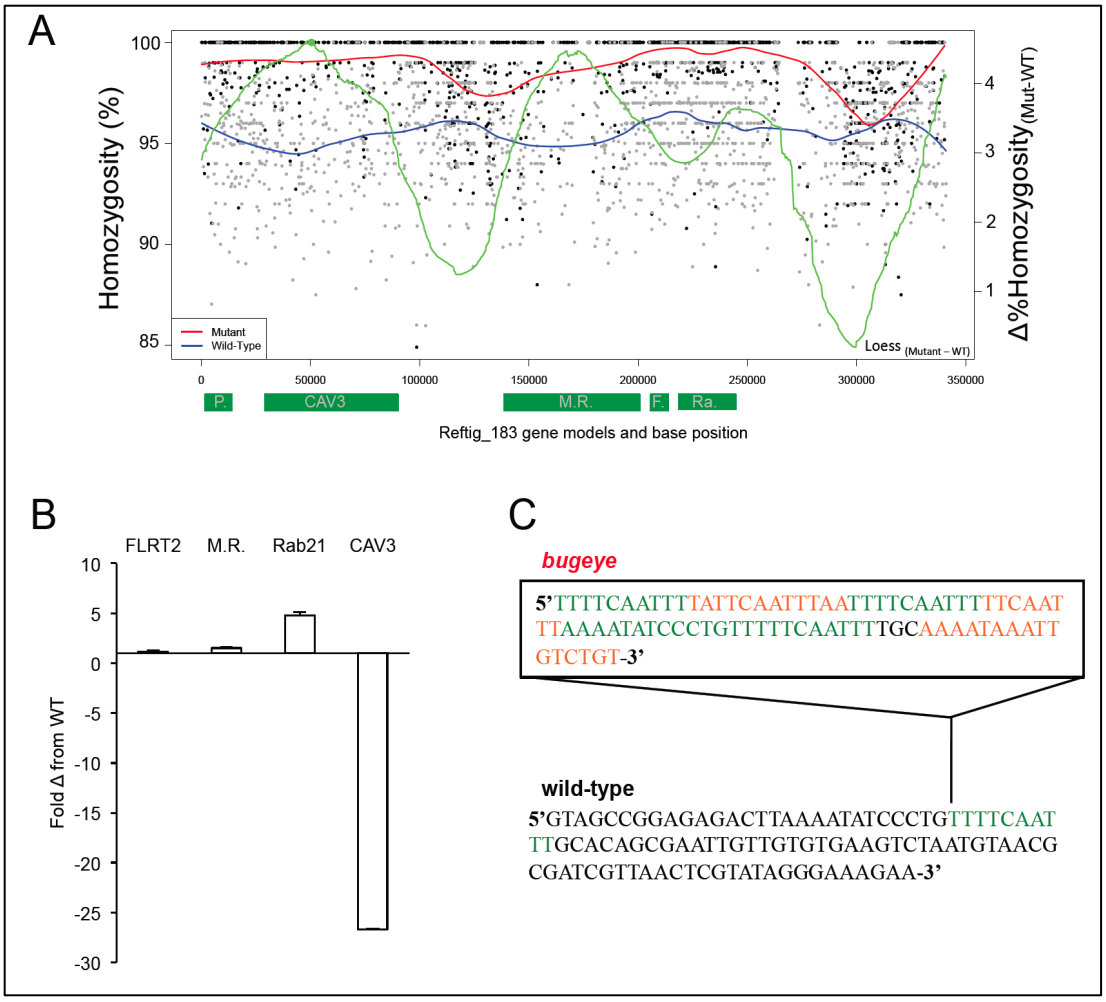

Figure 4. Homozygosity mapping on the *bugeye* ROI, reftig 183. **A)** Values were calculated for windows of 100 bp. Black points depict mutant values and gray points depict WT sibling homozygosity values. The differential value for the best fit lines of bug/bug (red) minus WT sibling (Blue) homozygosity is shown in green – the peak of this differential line is shown as a solid green point. Gene models and their approximate positions along reftig

183 are depicted along the X-axis as green rectangles. P = *phosholipid scramblase,* CAV3 = *CAV3,* M.R. = *cation-independent mannose receptor,* F.= *fibronectin leucine-rich transmembrane receptor 2,* Ra = *ras-related Rab21.* **B)** qRT-PCR of candidate genes on reftig 183. The plot shows the relative expression in *bugeye* compared to WT samples for the indicated genes. Expression levels were normalized to a housekeeping gene (RPS27A) first, and *bugeye* values were then compared to WT values in parallel reactions. Bar indicates average of three samples; error bars were calculated based on standard deviation in three biological replicates. **C)** Eighty-one bp insertion (box) found in the putative *cis*-regulatory region of the mutant *CAV3* gene. A repeating 10 bp element found in the insertion is shown in green.

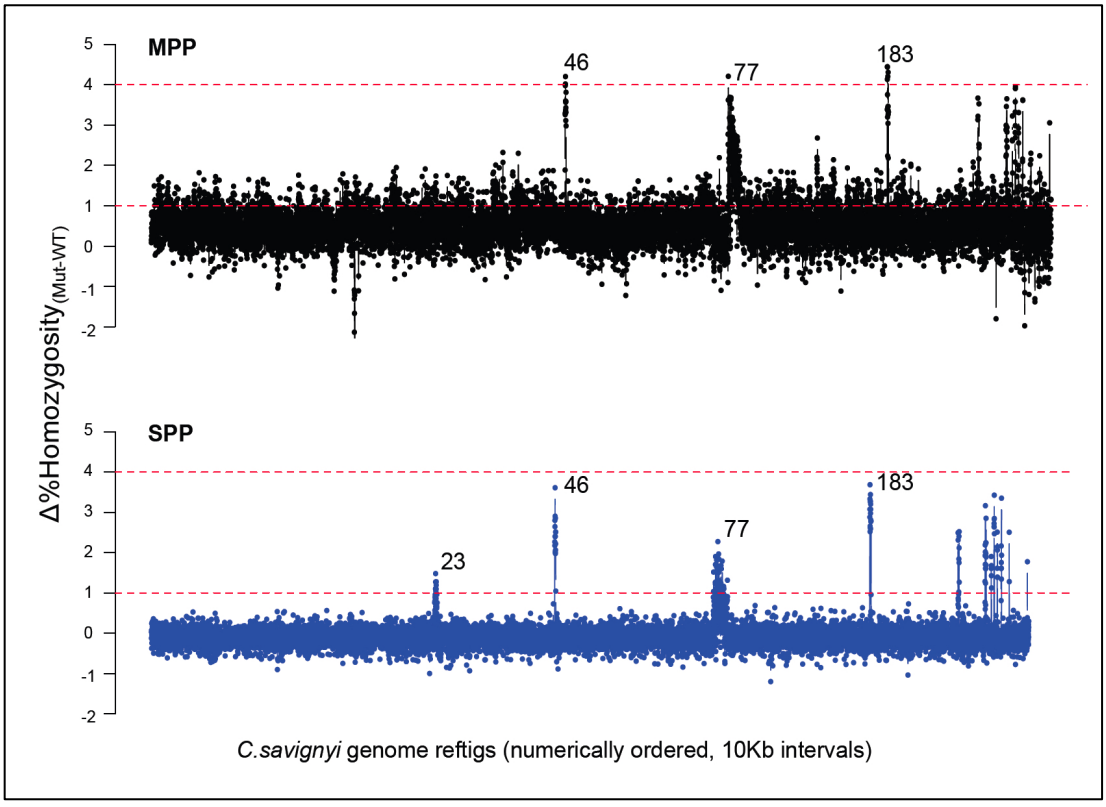

Figure 5. Comparison of outcrossed versus self-fertilized genomic datasets for mapping the *C. savignyi bugeye* mutation. MPP, multiple parents used for cross-fertilization and

progeny generation, data is shown in black. SPP, self-fertilized parent used for progeny generation, data is shown in blue. D% Homozygosity values were computed for 10 Kb windows across *C. savignyi* genomic reftigs. For the genome-wide plot, reftigs are presented in arbitrary order (according to assigned number) rather than as linkage groups. Reftigs smaller than 10 Kb were not included. Dashed lines represent reference lines at D1% and D4% Homozygosity values for comparing the two datasets. The three largest peaks fall on reftig 46, reftig 77 and reftig 183 in order. The extra peak seen in the SPP sample but not the MPP sample is reftig 23 (also known to belong to linkage group 11 (Hill et al., 2008)).

Supplemental Figure Legends

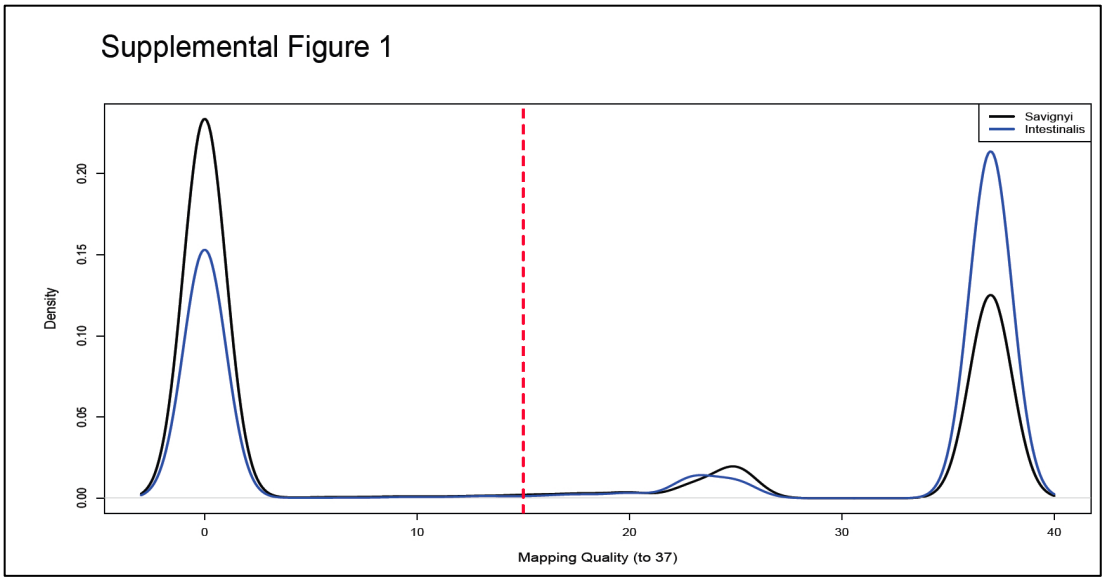

Figure S1. A probability density graph of distribution of read alignment mapping qualities in a *C. intestinalis (*blue line) and *C. savignyi* (black line) dataset is shown at bottom. Mapping qualities range from 0 to 37, with higher numbers meaning better quality alignment (Li et al., 2009). Red dashed line indicates the MapQ value of 15, which was used as the cutoff for mapping analysis.

Supplemental Figure 2

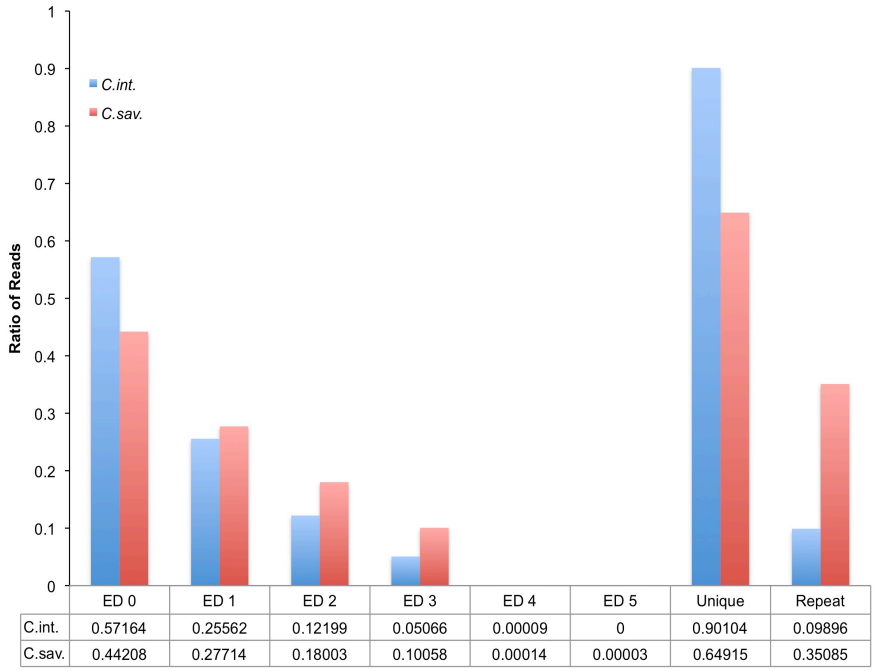

	ED 0	ED 1	ED 2	ED 3	ED 4	ED 5	Unique	Repeat
C.int.	0.57164	0.25562	0.12199	0.05066	0.00009	0	0.90104	0.09896
C.sav.	0.44208	0.27714	0.18003	0.10058	0.00014	0.00003	0.64915	0.35085

Figure S2. Comparison of Edit Distance (ED), and Unique versus Repeat character, of sequence reads between *C. intestinalis* (C.int.) and *C. savignyi* (C.sav.). The analysis was performed on a sample of 5 million randomly-picked reads. The values given for the two species represent the fraction of aligned reads with either the indicated ED assignment (0-5), or the Unique versus Repeat characteristic. Overall greater ED was observed in the *C. savignyi* sequence alignments in comparison to those from *C. intestinalis*. In addition, a greater fraction of *C. savignyi* reads were characterized as Repeats post-alignment. Both these factors, as well as others, contribute to the differential mapping quality of the two species (Li et al., 2009).

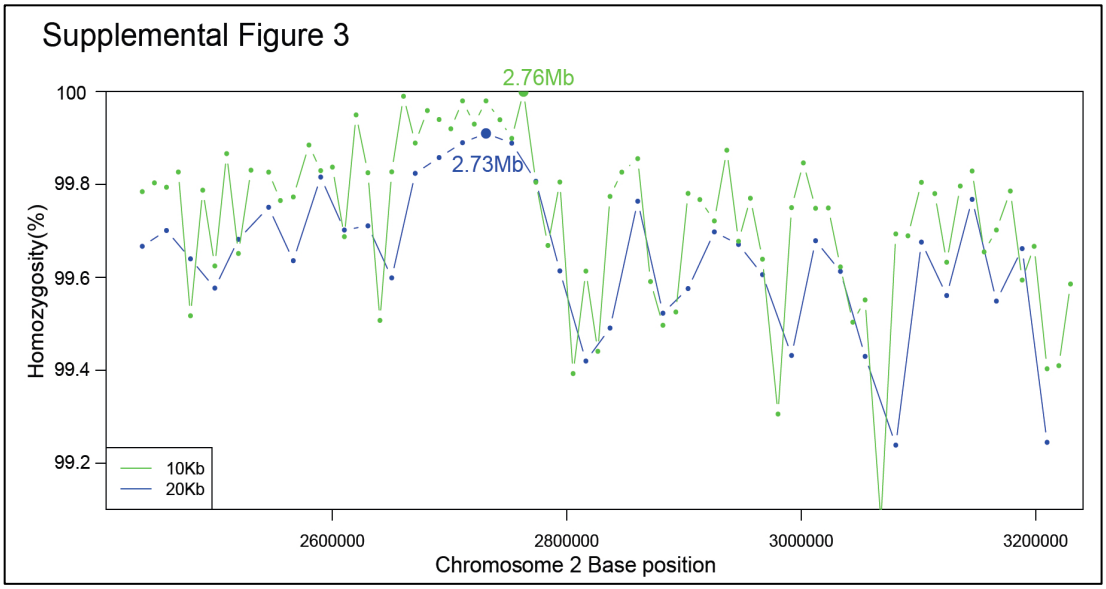

Figure S3. Window size differences for *C. intestinalis chongmague* genome-wide mapping. A zoomed in area of chromosome 2, near the peak calls for both a 10 Kb (green) and 20 Kb (blue) window analysis of homozygosity. Peaks of each analysis are shown as larger solid filled circles with positional values indicated next to each point.

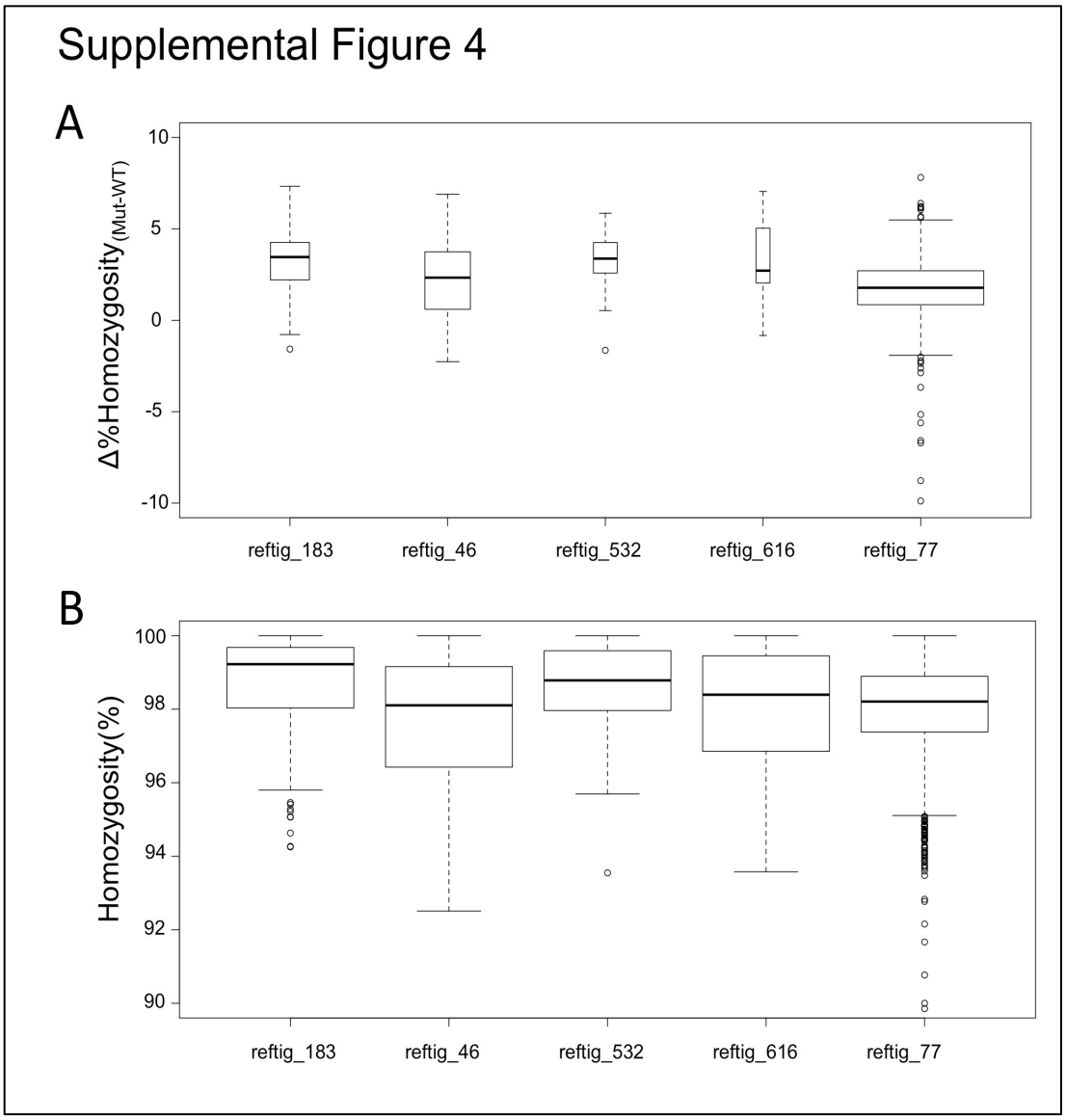

Figure S4. Homozygosity mapping analysis for *bugeye.* **A)** Box-whisker plot of Δhomozygosity values for each candidate high value reftig from Figure 2B. Δhomozygosity values were calculated for 1 Kb windows across each reftig. Width of boxplots depicts amount of data points for each reftig. Solid lines indicate median values, and whiskers indicate extreme values of reftig. Reftig 183 had the highest median Δhomozygosity value (3.46%)**. B)** Box-whisker plot of homozygosity values for the candidate reftigs (mutant sample only). Plots were done as above for panel A.

G. Tables

TABLE 1. *CIONA* DEEP SEQUENCING STATISTICS

Sample	**Total Reads**	**%Reads ≥ MapQ 15**	**Avg. Coverage**	**% of Sites ≥ 10X coverage**	**Avg. Homozygosity(%)**
C. intestinalis chm	159,931,687	68.5	34.22	95.42	98.23
MPP *C. savignyi* bugeye	116,448,947	37.4	13.62	67	96.97
MPP *C. savignyi* WT-sib	181,200,319	40.3	22.81	76.64	96.45
SPP *C. savignyi* bugeye	175,967,795	41.1	22.60	77.97	96.71
SPP *C. savignyi* WT-sib	166,735,236	39.6	20.63	74.42	96.78

TABLE 2. *BUGEYE* SEQUENCE CHANGES FOR *CAV3* GENE**.**

Genomic Position	**Mutation**
Promoter/5'UTR region	large insertion unique to mutant
45,007	D>N
45,011	I>T
46,850	T>R
47,973	M>T
50,330	Q>K
54,194	P>Q
55,701	E>K
66,750	S>C
66,926	A>S
68,702	T>A
69,589	E>D
90,325	C>S
90,811	3'UTR A>G
90,836	3'UTR C>A
90,858	3'UTR G>C

TABLE S1. DIFFERENCE IN COVERAGE BETWEEN CODING AND NON-CODING AREAS. Coding sequence regions were collected from Ensemble database (release 74) of each species' genome. A 5 Mb genomic region on Chromosome 1 of *C.intestinalis* and reftig 1 of *C.savignyi* were used for sampling differences in coverage in each sample.

Species	**CDS**		**non-CDS**		**Average**
	Coverage	Fraction of Average	Coverage	Fraction of Average	Coverage
C.savignyi	34.15	1.42	22.34	0.93	24.06
C.intestinalis	52.23	1.06	48.68	0.99	49.29

TABLE S2. PRIMERS FOR QRT-PCR

Gene	**Forward Primer**	**Reverse Primer**
ci-Actin	CCAGCAGATTCCATACCAAG	CGTTTTCCCATCCATCGTAG
ci-alpha Laminin PP#1	CGGTGACGAAAATGAGGAAC	AGACACCACCACCCTCGTAG
ci-alpha Laminin PP#2	TCAAGTTGGTTCCGCATGTA	GTTCCACATTCCACCAATCC
cs-CAV3 PP#1	GCGCATTTTGGTCATGCTAC	GGCTTGCCCACTTGATAATG
cs CAV3 PP#2	ACCATTTTGTTTTCGCCTTTT	ATTGAAGA**T**ATTGGGGTCCA
cs RPS27A	CCACCTGATCAGCAGAGGTT	TTATTCGCCCTCTGGTTTGA
cs Rab21	TTCGTGGTGGGAAATAAAGC	GTTTTCCGTTTTCACGCAAT
cs FLRT2	GTACACTGCTGCGAGGAACA	CCGTCTGATTGGTGGAAAGT
cs M.R.	CCGATGCTACGCCTATGACT	AGCCTCTACGTCGCCATCTA

III. Neural tube closure requires a T-type calcium channel gene

A. Abstract

We report that loss of T-type calcium channels causes anterior neural tube closure (NTC) defects in *Xenopus* and *Ciona*. With loss of T-type calcium channels there was no discernable defect in neural induction or neural fold formation. Rather, live imaging of embryos showed a failure to seal the anterior neuropore, suggesting a defect in adhesion. We observed a conserved aberrant upregulation of EphrinA effectors in *Xenopus* and *Ciona* accompanying the loss of T-type calcium channels. In wildtype *Ciona ephrinA-d* expression is down-regulated at the end of neurulation, and overexpression of EphrinA-d mimicked the T-type calcium channel loss of function phenotype. Furthermore, overexpression of a dominant negative Ephrin receptor was able to rescue NTC in *Ciona* T-type calcium channel mutants. We hypothesize signaling through T-type calcium channels modulates expression of genes, including *ephrinA-d*, and that down regulation of ephrinA signaling at the end of neurulation is necessary for proper anterior NTC.

B. Introduction

Neurulation, the process that transforms the neural plate into the neural tube, is a hallmark of the chordates. Although the details of neural tube closure (NTC) vary between species (Harrington et al., 2009), broadly conserved cytoskeletal mechanisms bring together the two lateral edges of the neural plate followed by their fusion at the dorsal midline. Disruption of NTC cellular mechanisms, such as those generating apically polarized constrictions in the epithelial neural plate cells, causes severe and sometimes irreparable defects in the spinal cord and brain (Haigo et al., 2003; Ybot-Gonzalez and Copp, 1999). Similarly, mutations that disrupt the planar cell polarity pathway genes, such as *dishevelled*

and *vangl2*, have been shown to disrupt convergent extension movements necessary for NTC (Murdoch et al., 2001; Wallingford and Harland, 2001). The final step of NTC is neural fold adhesion and fusion, and some key factors, such as the products of the *grhl2* and *N-cadherin* genes, have been found through reverse and forward genetic approaches (Bronner-Fraser et al., 1992; Pyrgaki et al., 2011).

Despite the wealth of studies, our understanding of NTC remains incomplete and insufficient to explain the spectrum of human NTC defects (Greene and Copp, 2014; Wallingford et al., 2013). We describe a new regulatory step in NTC that requires signaling through T-type calcium (Ca^{2+}) channels (TTCCs) for proper fusion of the closing neural tube. The requirement for T-type Ca^{2+} signaling appears to be late in NTC, and is distinct from earlier Ca^{2+} signaling events that are required for neural plate induction (Hackley et al., 2013; Leclerc et al., 2012), as well as from mechanisms of cell polarity and cytoskeletal-driven neural plate folding.

The original observation of the requirement for TTCCs in chordate NTC came from mapping analysis of mutant, *bugeye* (*bug*) in the ascidian *Ciona savignyi* (Abdul-Wajid et al., 2014). Here, we extend these observations from *C. savignyi*, and show conservation of this gene function during NTC in the amphibian *Xenopus laevis*.

C. Methods

Ciona Methods

Animals

Adult *Ciona* were collected from the Santa Barbara Harbor and maintained in constant light in flowing sea water tables. Transgenic lines were maintained at a culturing facility at

the University of California, Santa Barbara. Fertilized eggs used for electroporation and transgenesis were collected as previously described (Veeman et al., 2011b).

Transgenics and plasmids

Electroporation methods of *C. intestinalis* and *C. savignyi* were done as previously described (Veeman et al., 2011b). The *Ciona* CRISPR/Cas9 and U6 constructs were used as described (Stolfi et al., 2014). Guide RNA target sequences for *C. intestinalis* are listed in Supplemental Table 2, as well as the primer sequences used to detect the CRISPR mediated large deletion ('Mutdet' primers). Construction of a plasmid expressing EphrinA-d under the control of the ETR1 promoter (ETR>EphrinA-d) is detailed in supplemental procedures. Overexpression of EphrinA-d experiments used 50mg of ETR>EphrinA-d plasmid and 15mg of ETR>H2B:GFP . The control experiment used 65mg of ETR>H2B:GFP. ETR>GCaMP3 was made by similar Gateway methods from an Addgene plasmid of GCaMP3. ETR>GCamP3 was used at 75ug in C. savignyi electroporations.

EphrinA-d plasmid: EphrinA-d cDNA was isolated by PCR from *C. savignyi* cDNA with a kozak site added next to the translation start site (See Table 2 for primers). The PCR product was then TA cloned into PCR8 vector (Invitrogen) and then Gateway cloned into an ETR>rfa-myc vector. ETR>rfa-myc was made by ligating the ETR promoter(Tresser et al., 2010) into pSP72BSSPE-Swa1::RfA (Roure et al., 2007)with XbaI and StuI in 5' and 3' sites respectively.

The dominant negative EPH3 construct (ETR>dnEPH3) was made using primers (Supplemental primer table) to amplify dnEPH3 from Ngn>dnEPH3 (Stolfi et al., 2011). This amplicon was TA cloned into PCR8 (Invitrogen) and then Gateway LR reacted with the

ETR>rfa vector (Roure et al., 2007). The resulting plasmid (90 mg) was electroporated into clutches of embryos from heterozygous bug parents, as above.

Immunohistochemistry and Imaging

Ciona embryos were fixed in 4% PFA and filtered seawater. CRALBP, Arrestin and Opsin Antibodies were used as previously described in (Tsuda et al., 2003). Anti-PKCzeta antibody was used at 1:300 (Santa Cruz Biotechnology). Washing, secondary and clearing are as previously described (Veeman et al., 2008). Imaging of fixed *Ciona* samples was either on an Olympus FV1000 confocal or Olympus IX81. *Ciona* ETR>GCamP3 imaging was on the Olympus IX81 under a 20X water objective. Images were captured every 10 seconds for 30min-1hr intervals starting from neurula stages and ending in late tailbud stages of *C. savignyi*. Calcium transients were analyzed and quantified on Image J. In situ hybridizations were imaged on an Olympus BX51 with DIC optics and 20X objective. Fluorescent in situ hybridizations were cleared in glycerol and imaged on an Olympus FV1000 confocal under a 20X objective.

RT-PCR

C. savignyi bug mutants and wild type siblings larvae were collected for RNA as previously described(Abdul-Wajid et al., 2014). For comparisons of mutant and wild type by qRT-PCR equal amounts of total RNA used in each PCR reaction, and run as biological and technical triplicates. For the qPCR developmental time course, equal amounts of RNA were used for cDNA synthesis at each time point (200ng). Primers for qPCR are listed in Supplemental Table 2.

For single tadpole *Ciona* genomic PCR, genomic DNA was isolated as previously described (Veeman et al., 2011b) and primers are listed in Supplemental Table 2.

Drug Treatments

Mibefradil dihydrochloride (Sigma) was reconstituted at 4mM in filtered water, stored at 4 degrees. Nifedipine was used as previously described (Hackley et al., 2013) and equivalent amounts of DMSO were used as control in this experiment. Experimental concentrations were diluted in filtered seawater with antibiotics (Streptomycin and kanamycin) in a 3cm petri dish to which embryos of the appropriate stage were added. Embryos were washed of drug at the indicated stage through three changes of filtered seawater and allowed to develop in a new petri dish of filtered seawater and antibiotics.

Xenopus Methods

Animals

Females were induced for ovulation by a subcutaneous injection of human chorionic gonadotropin hormone as described (Sive et al., 2007). Eggs and sperm were collected for in vitro fertilization as described (Sive et al., 2000).

Morpholino injections

X. laevis CAV3.2 morpholinos (MOs) were designed according to the sequence Genbank entry GQ120631 and alignment with scaffold 22599 in *X. laevis* genome version 6 (xenbase.org). Two controls were used: the standard control morpholino (Gene Tools, CTL MO1) and a mismatch MO containing a 5bp mismatch from CAV3.2 splice disrupting morpholino 1 (CTL-MO2). Sequences for both CAV3.2 MOs and CAV3.2 mismatch MOs are in Supplemental Table 1.

Fertilized eggs were microinjected MOs at final doses of 40ng, 20ng and 10ng in a 10nl drop. After dose determination, subsequent embryos used for coronal section imaging or RNA isolation, were injected with a combination of CAV3.2 MO1 and MO2 at 40ng final, or

the CTL-MO2 at the same concentration. The same combination and concentrations of MOs were used in the GCamP3 co-injection experiments. The embryos were imaged for developmental defects from neurula to tailbud stages, then fixed in 4% Paraformaldehyde + MEM for immunohistochemistry or lysed in Trizol for RT-PCR analysis(Blackiston et al., 2010). RNAs for GCaMP3 were made from a gene construct using the T3 mMessage *in vitro* Transcription kit (Ambion), 1ng of RNA was co-injected with the MOs as indicated.

Immunohistochemistry and imaging

X. laevis embryos were fixed, embedded and sectioned as described (Blackiston et al., 2010). Primary antibody sera to NCAM (4d-s) and E-cadherin (5D3) were obtained from the Developmental Studies Hybridoma Bank at University of Iowa and used at final concentrations of 5mg/ml. Fluorophore conjugated secondary antibodies (Invitrogen) were used at 1:500. Sections were mounted in glycerol.

For GCamP3 imaging, GFP expressing embryos from each experimental condition were placed in 1% low melting pointing agarose and 1/3X MMR on a coverslip-bottom dish. Embryos were oriented with neural plates facing down and then imaged on an inverted Zeiss 780 LSM or an Olympus FV1000. Imaging was done with a 20X objective and images captured every second for 8-10 minutes. The analysis of GCamP3 images was done with ImageJ and described in supplemental procedures.

GCamP3 imaging analysis: Fields of view were position-corrected for drift and then regions of interest (ROI) were manually created for 10-20 cells. Mean fluorescence values were extracted for each ROI and tabulated in Microsoft Excel. Averaging the mean fluorescence for an ROI over time and then dividing each individual time point mean

fluorescence by the average generated relative fluorescent intensity values. An increase of 30% was defined as a Ca^{2+} transient.

RT-PCR

Primers used for RT-PCR on *X. laevis* single tadpole cDNA are listed in Table 2. Single embryos were lysed in TRIZOL for RNA isolation and 400ng of total RNA was used to make cDNA (Invitrogen Superscript III).

GCaMP3 imaging analysis

Fields of view were position-corrected for drift and then regions of interest (ROI) were manually created for 10-20 cells. Mean fluorescence values were extracted for each ROI and tabulated in Microsoft Excel. Averaging the mean fluorescence for an ROI over time and then dividing each individual time point mean fluorescence by the average generated relative fluorescent intensity values. An increase of 30% was defined as a Ca^{2+} transient.

Statistics

Standard T-tests were used for normal distributed transcript expression data in *Ciona* and *Xenopus*. For the binary event of open vs closed brain in wild-type *Ciona* embryos, a Fisher exact test was used to determine significance. However in the rescue experiment of the *Ciona bugeye* mutants, a chi squared test was used to determine significant changes from the expected mean of 25% open brain phenotypes in the control scenario even though the read out was still a binary event (open versus closed brain).

D. Results

Loss of CAV3 results in an open anterior neural tube

In a screen for spontaneous mutants in wild-collected *Ciona savignyi* (Veeman et al., 2011b) we identified a recessive line (*bugeye*) with an open brain phenotype, and mapped the

causative mutation to the *cis*-regulatory region of the single TTCC gene (CAV3) of the *C. savignyi* genome (Abdul-Wajid et al., 2014). Further experiments showed that the expression level of CAV3 was greatly reduced in homozygous *bug* mutants relative to their wild type siblings, suggesting that deficient Ca^{2+} signaling through the CAV3 channel was responsible for the open brain phenotype. To investigate this possible causative link further, the CAV3 gene in the closely related species *Ciona intestinalis* was targeted using CRISPR/Cas9 genome editing (Ran et al., 2013). Like *C. savignyi*, *C. intestinalis* has only a single CAV3 gene (Okamura et al., 2005b). We targeted the *C. intestinalis* CAV3 gene using two guide RNAs complimentary to exon 3 and 49. Nuclear Cas9 was expressed using the ubiquitous EF1alpha promoter (Stolfi et al., 2014). The eggs also received the plasmid ETR1>H2B:GFP to mark cells of the central nervous system (CNS) (Veeman et al., 2010). At the late tailbud stage a *bugeye(bug)-like* phenotype (i.e., open brain) was observed in 17% of the electroporated embryos (n=362), versus 3% (n=374) of embryos receiving a control guide RNA (Figure 1A and B) (p=0.0001 Fisher Exact). If both CAV3 guide RNAs cleaved the target sequence successfully, an expected deletion of ~23Kb of DNA from *C.intestinalis* CAV3 gene would be produced. Using PCR primers spanning the outer edges of the target sites, a ~130bp PCR product was detected in the *bug-like C. intestinalis* embryos, but not in the control guide RNA electroporated embryos (Figure 1C). Sequences of several cloned PCR products confirmed they were generated from the targeted region, and that they contained large and variable deletions (Figure 1D).

CNS cells in the bug *mutant are differentiated and polarized*

NTC defects, whether genetic or environmental, can be placed into two broad, and non-mutually exclusive, categories: those that arise from failure of neural tube differentiation, and those that arise due to defects in the mechanics of neural tube folding and/or adhesion (Wallingford et al., 2013). In *C. intestinalis* we previously characterized the mutant *frimousse*, which causes severe defects to the anterior neural tube, including a failure in brain closure (Deschet and Smith, 2004; Hackley et al., 2013). This mutation, the product of a lesion in a connexin gene, results from a failure to maintain neural induction in the anterior neural plate, and is evident in the loss of expression of anterior CNS genes, and in the aberrant expression of an epidermal gene in the mis-specified brain. In contrast to *frimousse*, in *bug* we observed comparable immunostaining of the pan-neural protein CRALBP, and the brain-specific proteins Opsin and Arrestin (Tsuda et al., 2003) in wild type and mutant larvae (Figure 2A and B). In addition to the CNS, the adhesive palps in *bug* mutants were indistinguishable from wild type. In *Ciona* the palps are derived from the anterior-most region of the neural plate (Nishida, 1987; Veeman et al., 2010), and in *frimousse* embryos they are absent.

Mechanically, NTC is characterized by the formation of apically polarized actin filaments. The action of these polarized filaments results in the apical constriction of the cells and the folding of the neural plate inward. Disruption of this actin machinery and/or accessory proteins can cause neural tube closure defects (Wallingford, 2005). In *C. savignyi* we observed that antibody staining for the apically localized cell polarity protein aPKC (Ghosh et al., 2008; Solecki et al., 2006) labels the surface of the CNS lumen (Figure 2C). In the *C. savignyi* brain periluminal staining can be seen in both the sensory vesicle and visceral ganglion (*Ciona* orthologs of the fore- and hindbrains, respectively), as well as in the

neurohypophysial duct, which joins the sensory vesicle to the stomodeum *(Manni et al., 2005). In bug mutants we observed strong aPKC staining throughout the CNS, although anterior staining of the sensory vesicle was splayed outward in the open brain rather than forming a closed lumen (arrowheads Figure 2D). Similarly, phalloidin labeling of bug mutants showed strong polarization of actin to the* apices *of cells in the CNS, including cells in the open anterior brain, of comparable intensity to phalloidin labeling in wild type embryos (Figure 2E versus 2F, red staining and yellow arrows). In summary,* the CNS of *bug* mutants has no conspicuous defects in neural induction and specification, or in the formation of apically polarized cells

Onset of bug *phenotype*

An important clue to the nature of the mechanism of the *bug* mutation comes from the observation that the phenotype, an open anterior neural tube, does not become apparent until after the late tailbud stage, when neural tube closure in wild type embryos is complete. At stage 25 (late tailbud) sagittal confocal sections of *bug* embryos show that the anterior neural tube closure is largely complete, with most of the brain covered in epidermis, but with an enlarged anterior neuropore (yellow arrowheads Figure 3A and B). Additionally, the two pigmented cells that comprise the ocellus and the otolith (Jiang et al., 2005b) are misplaced in *bug* to the opening of the neuropore rather than in the brain vesicle (red asterisks Figure 3B). To better visualize the developing CNS, the *bug* line was crossed with a stable transgenic line expressing GFP under the control of the pan-neural ETR1 promoter. Time-lapse movies of *bug* embryos confirm that the brain is initially covered with epidermis (i.e., relatively normal brain closure and neurulation), and that, over the course of approximately 4

hours, the brain erupts from the anterior neuropore by hatching larva stage (Figure 3C and C', and Supplemental Movie 1). These data demonstrate that the late step of anterior neuropore sealing is defective in *bug* embryos (whereas earlier neurulation is normal), and that this results in the opening and protrusion of the initially epidermis-covered brain.

Temporal T-type Ca^{2+} *channel function*

To better understand the temporal requirement for CAV3 in neural tube closure, embryos were treated at various time points with the TTCC-blocking drug mibefradil (Martin et al., 2000). Preliminary experiments confirmed that mibefradil treatment of neurulating embryos closely phenocopies *bug*, while the L-type channel blocker, nifedipine, gives a much different phenotype (Figure 3D and 3E). Treatment of embryos with mibefradil during short temporal windows identified the period of sensitivity for anterior neural tube closure: between neurula and mid-tailbud stages (Figure 3F). Thus, there is a lag time of ~5hrs from when CAV3 function is required (between stage 16 and 21) and the stage at which the phenotype becomes fully evident (stage 25 onward) suggesting an early tailbud CAV3-dependent signal which plays a role in the later sealing of the anterior neuropore.

Xenopus *requires a T-type* Ca^{2+} *channel to close the anterior neural tube*

X. laevis has three orthologs of *Ciona* CAV3: CAV3.1, 3.2 and 3.3. CAV3.2 is the earliest of these to be expressed in the neurulating embryo (Lewis et al., 2009). To determine if this gene has a conserved role with its *Ciona* ortholog in neurulation, we used morpholino oligonucleotides (MO) to knock down its expression. Two splice-blocking MOs to *X. laevis* CAV3.2 were tested (CAV-MO1 and CAV-MO2), as well a two control MOs [standard

control MO (Genetools), and custom mismatch MO]. Both CAV3.2 MOs produced open brain phenotypes in 80-100% of injected embryos (albeit at different dose efficacies), while no neurulation defects we observed with either control MO (Figure 4A). RT-PCR confirmed the efficacy of the MOs in blocking splicing and down-regulation of spliced transcript (Figure 4B).

The defect caused by the CAV3.2 MOs can be seen in representative embryos at stage 22 as a failure of the anterior neural folds to fuse (Figure 4C and D). The defect is not simply a delay, as no fusion of the anterior folds is seen with extended culturing. In fact, by stage 26 we observed in 17% of 58 CAV-MO1 injected embryos that material (possibly brain) erupted from the open neural pore (Figure 4E and F; Supplemental movie 1). The remainder of the CAV3.2 MO1 injected embryos at stage 26 showed severe head malformations with a deep dimple at the hindbrain (Figure 4G).

As in the *Ciona bug* mutant, we observed no general defect in neural induction for *X. laevis* embryos injected with the CAV3.2 MOs based on NCAM antibody staining, although anterior closure was clearly defective (Figure 4H-J; stage 24 embryos). Immunostaining for E-cadherin, which marks the epidermis in *X. laevis*, showed that even where the anterior neural tube was splayed open in the CAV3.2 MO embryos, an abnormal covering of epidermis was found over and into the open neural folds (Figure 4K-M). These results demonstrate that *X. laevis* embryos also require a TTCC gene, CAV3.2, to effectively close, but apparently not to specify, the anterior neural tube.

CAV3 expression in Ciona

The results above suggest a conserved functional role for TTCCs in chordate neural tube

closure. To further examine conservation between the two genes, their spatial expression was compared. The expression of the *X. laevis* CAV3.2 gene has already been described (Lewis et al., 2009). At developmental stages relevant for neural tube closure (as early as stage 20), *X. laevis* CAV3.2 expression is observed along the lateral edges of the developing neural folds and tube. This expression extends the length of the neural tube and increases into fore, mid and hindbrain regions at later stages (24-36) as well as into the presumptive heart tissue (Lewis et al., 2009). For *C. savignyi* the expression of the CAV3 gene was investigated by *in situ* hybridization. No specific signal could be detected until early tailbud stage [*Ciona* stage 19 (Hotta et al., 2007)]. At this stage the most conspicuous hybridization was observed in a cluster of cells that appear to correspond to the midbrain-hindbrain boundary (MHB) region and in the caudal nerve cord (Figure 5A). Based on the conserved expression patterns of *otx*, *engrailed*, *pax2/5/8* and *fgf8/17/18* in the brain, *Ciona* is thought to have a structure equivalent to the midbrain–hindbrain organizer (Raible and Brand, 2004). Expression of *C. savignyi* CAV3 increased in intensity in the MHB region at mid- and late-tailbud stages, and new expression was observed both in the forebrain (arrows in Figure 5B-D) and in a small patch of cells in the epidermis overlaying the sensory vesicle, posterior to the anterior neuropore (arrowheads in Figure 5C and D). Double fluorescent in situ hybridization confirms that the expression of *engrailed* and *CAV3* overlap in the *C. savignyi* MHB region (Figure 5E-G).

Ca^{2+} transients in neurulating embryos

Calcium transients in the developing neural plate and tube of both *Ciona* and *Xenopus* have been well documented. We described the presence of gap junction-dependent Ca^{2+}

transients in the neural plate of *C. intestinalis* (Hackley et al., 2013), and in *Xenopus* Ca^{2+} transients via the DHP-sensitive CAV1 family play a critical role in neural induction [reviewed in (Leclerc et al., 2012)]. However, TTCC transients in the neurulating chordate CNS have not been reported. To investigate this, one-cell stage *X. laevis* embryos were injected with the RNA encoding the Ca^{2+} indicator GCaMP3 (Tian et al., 2009) and either control or CAV3.2 MOs. Live imaging was centered to the anterior closing neural folds of neurula stage embryos, where neural tube closure defects were observed and CAV3.2 expressing cells are present (Lewis et al., 2009). In a single plane of view of control MO embryos we could detect Ca^{2+} transients in ~50% of the cells in the field of view, with each transient lasting on average 33 seconds (Figure 6A-C, Supplemental movie 3). The number of cells having transients, and the length and the intensity of the transients was reduced in CAV3.2 MO embryos (Figure 6B, asterisks indicate significance of $p \leq 0.05$, Supplemental movie 4). However, no difference was detected in the frequency of the transients (Figure 6B). Thus CAV3.2 is required for normal Ca^{2+} transients in the developing *X. laevis* anterior neural tube.

At early tailbud stages in *C. savignyi* we observed a strong correlation between CAV3 expression and Ca^{2+} transients using an electroporated construct with the ETR1 driver for GCaMP3 (Hackley et al., 2013). Starting at early tailbud stage, GCaMP3 Ca^{2+} transients were observed in the MHB region (Figure 6D and 6E; Supplemental Movie 4), and continued through the mid tailbud stage. The MHB transients diminish after mid tailbud stage (data not shown).

T-type Ca^{2+} channels and ephrin regulation

The characterization of the TTCC phenotypes in both *Ciona* and *Xenopus* suggest that the neural tube closure defects arises not from a deficiency in neural induction or neural tube folding, but rather from a later event, perhaps one involving cell adhesion and/or neuropore sealing. In mouse, EphrinA-EphA interactions have been shown to be important for neural fold fusion (Abdul-Aziz et al., 2009). We investigated expression levels of the *C. savignyi* ortholog of this gene, *ephrinA-d* (Picco et al., 2007), as well as Neural Cell Adhesion Molecule (NCAM), and the neural-specific genes *otx*, *six3/6*, and *etr1* (Takamura et al., 2001) at late tailbud stages in wild type and *bug* mutants by quantitative RT-PCR . The ubiquitously expressed gene *RPS27A* was included as a control (Olinski et al., 2006). While there was no difference in expression of NCAM and ETR1 between wild type and *bug*, *ephrinA-d* was up-regulated approximately 1.6 fold in the mutant relative to wild type. In these same *bug* embryos we observed down-regulation of the anterior neural genes *otx* and *six3/6* (Figure 7A). Because of the role of EphrinA in mouse neural tube closure and the strikingly similar in-situ pattern of *ephrinA-d* in *Ciona* to our *CAV3* in-situ (Imai et al., 2009), the *C. savignyi ephrinA-d* up-regulation result was of particular interest. In *C. intestinalis*, *ephrinA-d* has been shown to be necessary for the proper patterning of the neural plate, although a later role in neural tube closure has not been reported (Haupaix et al., 2014; Stolfi et al., 2011). We examined the normal developmental time-course of *ephrinA-d* expression by qRT-PCR. Several peaks in *ephrinA-d* expression were observed: at 32-cell, gastrula and early tailbud stages consistent with the previously published in-situ data (Figure 7B) (Imai et al., 2009). Of potential significance is a dramatic down-regulation of *ephrinA-d* expression from early through late tailbud stages in wild type embryos.

We also examined ephrinA signaling in *Xenopus* embryos. The ephrinA receptor EPHA2 is known to be expressed in the developing *X. laevis* neural tube (Brandli and Kirschner, 1995). A significant increase in the transcript for EPHA2 was observed in *X. laevis* embryos injected with the CAV3.2 MO relative to controls (Figure 7C, EPHA2 significance p=0.025, T-test), while no change was observed for *NCAM* expression (nor for *actin* and *histone 4*). While there are several EphrinBs expressed at this stage, their effects on the neural tube appears to be on apical constriction rather than adhesion (Ji et al., 2014).

To investigate if mis-expressing EphrinA-d in *Ciona* in the late tailbud *Ciona* embryos could replicate the *bug* phenotype, 1-cell stage embryos were electroporated with a plasmid containing the *ephrinA-d* cDNA driven by the ETR promoter, which expresses through the late tailbud stage in *C. savignyi* (Tresser et al., 2010). A significant fraction of embryos electroporated with the EphrinA-d construct had an open brain phenotype compared to controls overexpressing nuclear GFP under the same promoter (15.2%, versus 4.8% in controls, p=0.0006 Fisher Exact) (Figure 7D and 7E versus 7F).

Rescue of bug *embryos by ephrinA inhibition.*

Based on the expression and over-expression data, we hypothesized that failure of *bug* embryos to properly down-regulate *ephrinA-d* late in neurulation could cause the open-brain phenotype. To test this hypothesis directly, we asked whether inhibition of EphrinA-d could restore anterior neural tube closure in *bug* embryos. For these experiments a previously characterized dominant negative version of the receptor for EphrinA-d, EPH3, (Haupaix et al., 2013; Picco et al., 2007) was expressed by electroporation in the CNS of *Ciona bugeye* embryos using the ETR1 promoter. Because the *bug* allele is lethal when homozygous

(Abdul-Wajid et al., 2014) embryos are generated by crossing heterozygous adults. In clutches of *bug* embryos electroporated with the control plasmid, the *bug* phenotype was observed at close to the expected frequency of 25% (Figure 8A). In these experiments four independent clutches of embryos were electroporated, and the frequency ranged from 23.1% to 25.4% (average 23.9%, n=300, chi squared test p=0.689). In contrast, for embryos from the same clutches electroporated with the dominant negative EPH3 (dnEPH3) the frequency of observed *bug* phenotypes ranged from 15% to 21% (average 17.1%, n=361, chi-squared test p=0.002), indicating that anterior neural tube closure had been rescued in a portion of the *bug* embryos.

To further investigate the possible *bug* rescue, individual embryos were genotyped. The *bug* allele contains an 80bp insertion that can readily be identified by gel electrophoresis of PCR-amplified genomic DNA from single embryos (Figure 8B). In a preliminary experiment, the link between the *bug* phenotype and the genomic insertion was confirmed (Supplemental Figure 1). In forty-five embryos examined, the *bug* phenotype was only observed in embryos homozygous for the insertion. Importantly, closed anterior neural tubes were never observed in those embryos homozygous for the insertion, nor were open neural tubes observed in those embryos genotyping as heterozygous, or genetically homozygous wild type. For clutches electroporated with the dnEPH3 construct, twelve embryos scored as having closed anterior neural tubes were genotyped. In contrast to the results for control embryos, three of these embryos genotyped as homozygous for the *bug* allele (Figure 8B), indicating that they were rescued. Note also that the example rescued *bug* embryo (yellow arrow in number 6, Figure 8B) has extra pigment cells, a previously described phenotype of dnEPH3 expression (Haupaix et al., 2014). Finally, we observed a number of embryos that

appeared to be partially rescued by dnEPH3 (Figure 8C). These were scored as having open neural tubes for the data shown in Figure 8A.

E. Discussion

The present study shows a requirement for TTCC signaling in NTC for both ascidians and amphibians, suggesting that this is an ancient function that predates the split of the vertebrates and the tunicates. Zebrafish CAV3.2 is also expressed during neurulation with a partially overlapping pattern to *Xenopus* [zfin.org, probe cb648, (Lewis et al., 2009)]. The nature of the defects reported here for loss of T-type Ca^{2+} function in *C. savignyi*, *C. intestinalis* and *X. laevis* are consistent with it playing a role in the fusion/adhesion of neural folds, rather than in neural specification or neural fold generation. In *C. savignyi* the open anterior neuropore led to a dramatic eruption of the brain from the head of homozygous *bug* mutants. In *X. laevis* we observed a less frequent, but similar, expulsion of tissue from the open neuropore of CAV3.2 knockdown embryos.

The CAV3 family consists of three vertebrate members (CAV3.1, 3.2 and 3.3) and a single member in tunicates (Abdul-Wajid et al., 2014; Okamura et al., 2005b; Perez-Reyes and Lory, 2006). This family of Ca^{2+} channels is characterized by rapid opening in response to small membrane depolarizations (Perez-Reyes, 2003). While TTCCs have most thoroughly been investigated in adult tissues such as the heart and neurons, these channels are expressed embryonically (Frischknecht and Randall, 1998; Gottmann et al., 1988). Recent studies have demonstrated that CAV3.2 in mice initiates differentiation cascades in early embryonic tissues including in neural progenitors, heart and skeletal muscle (Berthier et al., 2002; Ferron et al., 2011; Louhivuori et al., 2013). It has also been demonstrated that

TTCC activity can directly initiate transcriptional programs in chondrocyte differentiation (Lin et al., 2014).

Results presented here show that loss of TTCC function aberrantly upregulates the expression of EphrinA-d and EPHA2, in *C. savignyi* and *X. laevis*, respectively. Although in mouse EphrinA signaling has been reported to promote neural tube fusion (Abdul-Aziz et al., 2009), and loss of ephrinA5 in mice leads to a failure of neural tube fusion (Holmberg et al., 2000), this same pathway in other contexts can lead to cell repulsion (Arvanitis and Davy, 2008). Moreover, results presented here show that overexpression of *ephrinA-d* can lead to an open brain phenotype in *C. savignyi*. Thus the actions of this pathway (adhesive or repulsive) may depend on the temporal context and/or the relative concentrations. Consistent with this, we observed in *C. savignyi* a spike in *ephrinA-d* expression in the early tailbud embryo, corresponding to the onset of neural fold fusion. However by late tailbud stage, ephrinA-d transcript levels fall dramatically, suggesting that any requirement for ephrinA-d in neural fold fusion is transient. Moreover, the ability of dnEPH3 to rescue *bug* embryos indicates that the down regulation of *ephrinA-d* is necessary for proper anterior neuropore closure. A summary model of our results on CAV3 function and EphrinA during neurulation is presented in Figure 9.

The CAV3-EphrinA relationship is more complicated in *X. laevis*. While the temporal and spatial expression of all five EphrinA ligands, and ten EphrinA receptors, has not been described, two *X. laevis* EphrinA receptors, EPHA2 and EPHA4 have distinct expression patterns in the neural tube and partially overlap with CAV3.2 expression (Brandli and Kirschner, 1995; Park et al., 2011; Smith et al., 1997) (XDB3, http://Xenopus.nibb.ac.jp). However there remain many uncharacterized EphrinA ligands and receptors, and the two

Xenopus TTCCs not examined here, CAV3.1 and CAV3.3, are also expressed at later stages of neural tube closure, and are partially redundant with CAV3.2. Redundancy may explain why no NTC defect is reported in the CAV3.2 knockout mouse (Chen et al., 2003). However, the present results suggest that neural fold fusion in these mice should be reexamined.

Finally, CAV3.2-dependent Ca^{2+} transients were observed in the *X. laevis* neural tube. In adult nerve, muscle, and cardiac cells TTCC activation, and the resulting Ca^{2+} entry, is tied to specific physiological/sensory stimuli (Nelson et al., 2006). However, the embryonic nervous system is characterized by early spontaneous ion channel activity [reviewed in (Leclerc et al., 2012; Rosenberg and Spitzer, 2011)]. Thus the CAV3.2-dependent Ca^{2+} transients in the closing *Xenopus* neural tube could be the products of either spontaneous activity, or possibly a sensory signaling event. One possible role of TTCCs in NTC could be to monitor the mechanical progress and/or quality of NTC. Interestingly, in adult proprioceptive nerves, CAV3.2 has been found to be essential for low-threshold mechanoreception (Francois et al., 2015). Future experiments will investigate the potential roles of spontaneous versus sensory activation of TTCCs in NTC.

F. Figures and Figure Legends

Figure 1.

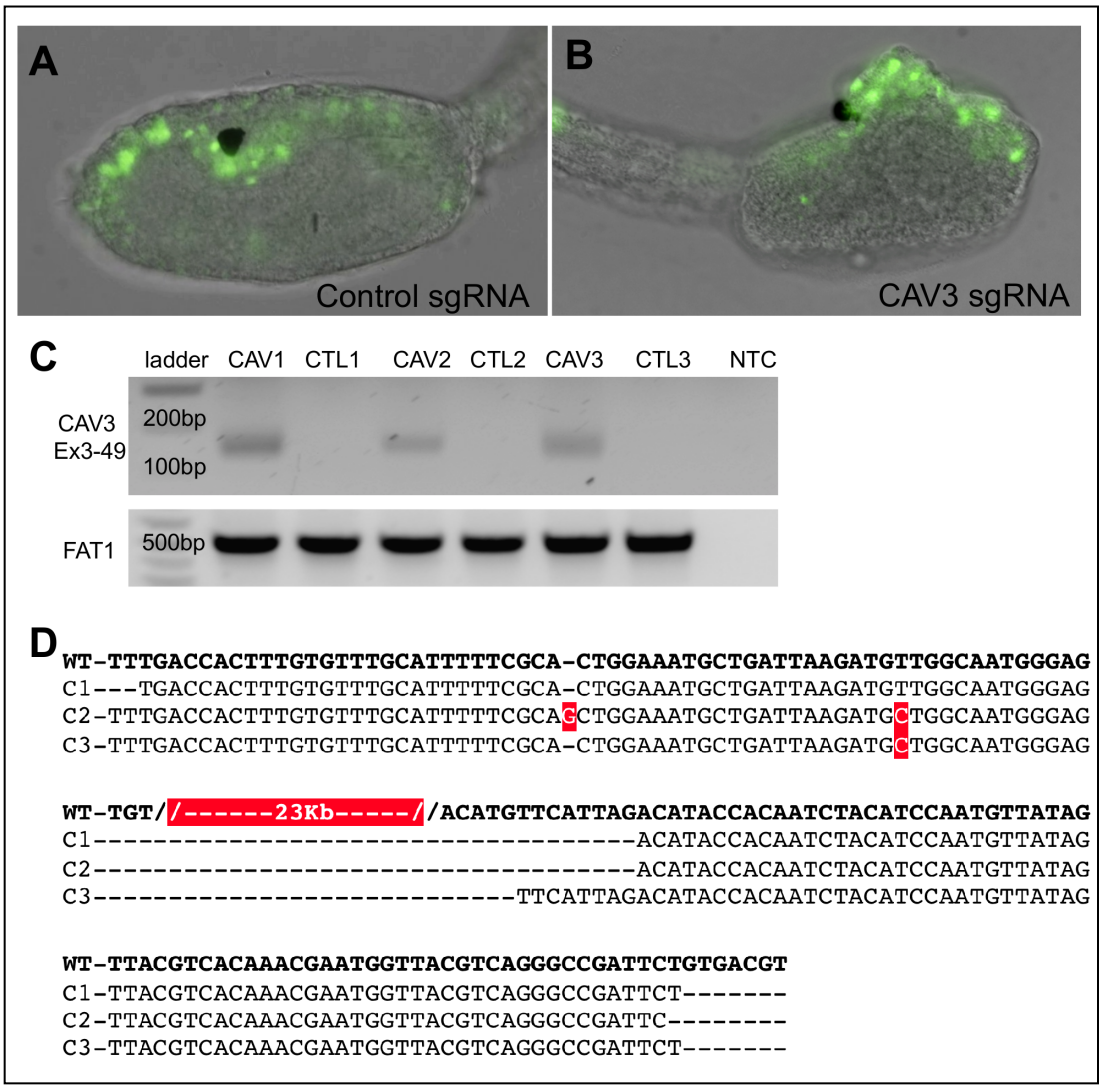

Figure 1. CAV3 is required for *Ciona intestinalis* neural tube closure. **A** and **B**. Representative *C. intestinalis* embryos expressing a control guide RNA (sgRNA) (**A**), or guide RNAs targeting exons 3 and 49 of the *C. intestinalis* CAV3 gene (ciCAV3 sgRNA) (**B**). Green fluorescence from a pan-neural ETR1 promoter driving nuclear GFP construct marks neural tube cells. **C.** Genomic PCR of the region target by CRISPR/Cas9 genome editing. Genomic PCR results from three embryos receiving the control sgRNA (CTL1-3),

and three receiving the ciCAV3 sgRNAs (CAV1-3) are shown. Only in the CAV3-targeted embryos is the expected deletion product detected. Amplification of the unlinked Fat1 gene serves as a control for DNA input. **D.** Nucleotide sequence verification of CRISPR/Cas9 deletions in the *C. intestinalis* CAV3 gene. The sequences from three subcloned PCR products are shown (cln1-3). The PCR products align to both exon3 and exon49 of CAV3 confirming an expected ~23Kb deletion.

Figure 2.

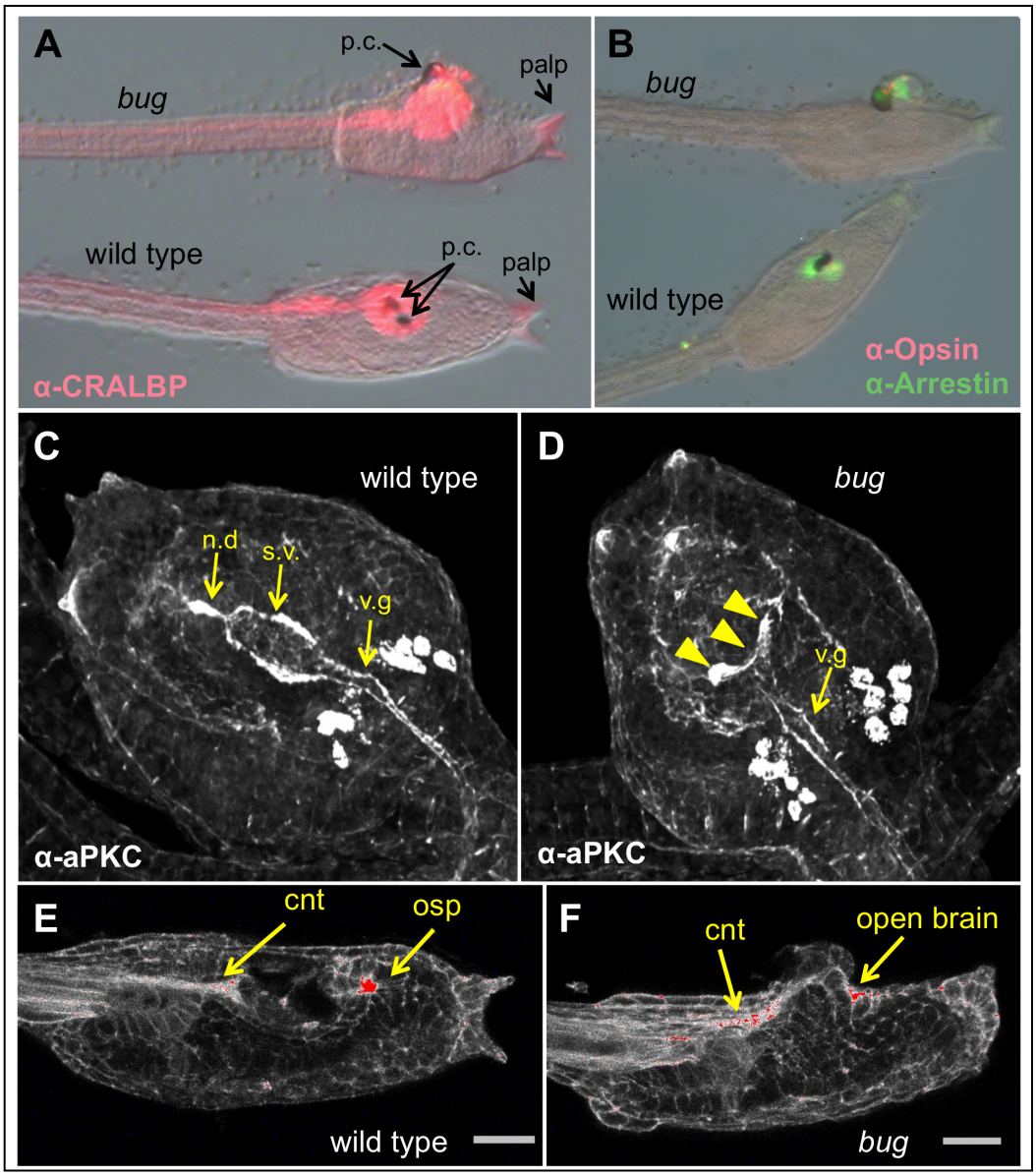

Figure 2. *Bug* mutants differentiate and polarize the anterior neural tube. **A** and **B**. *Bugeye* (*bug*) and wild type siblings stained for the neural markers CRALBP, Opsin and Arrestin, as indicated. **C** and **D**. Immunostaining for the cell polarity marker aPKC in wild type and *bug* mutants. s.v. = sensory vesicle, n.d.= neurohypophyseal duct, v.g.= visceral ganglion. The staining intensity is consistent between *bug* and wild type, although the

sensory vesicle in *bug* embryos is open (arrowheads in D). Views are dorsal. **E** and **F**. Phalloidin staining of *bug* and wild type sibling larvae. The most intense staining is in red. cnt= caudal neural tube, osp=oral siphon primordium. Scale bar = 24 mm.

Figure 3.

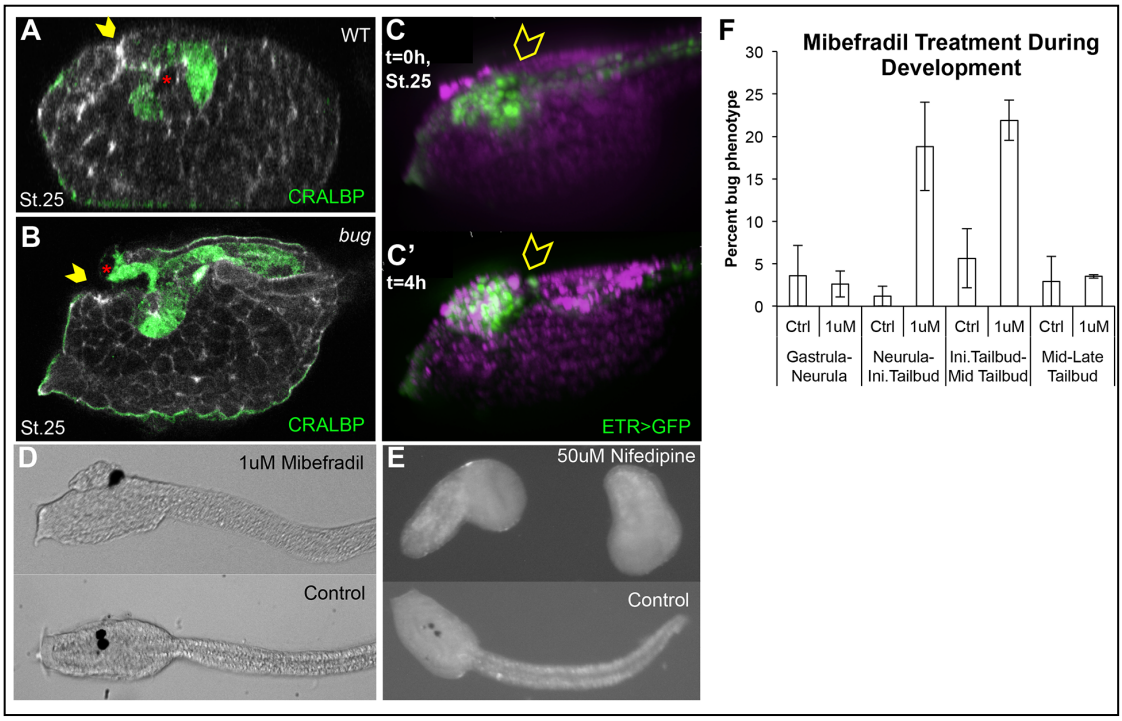

Figure 3. Onset of open brain phenotype in *Ciona*. **A** and **B**. Mid-sagittal confocal sections of late tailbud (stage 25) *bug* and wild type (WT) sibling embryos showing immunostaining for CRALBP. Yellow arrowheads indicate the anterior neuropore. The pigmented cells of the sensory vesicle are indicated by red asterisks. **C** and **C'**. Still images from the start and end of Supplemental Movie 1 of a *bug* embryo. Cells of the neural tube express GFP from the pan-neural ETR1 promoter. Magenta indicates FM464 stained membranes. Yellow arrowheads indicate sensory vesicle that, at the start of movie (**C**; t=0) is covered by non-neural tissue (i.e., epidermis), and then at four hours (**C'**; t=4h) is exposed on the surface. (A-C': lateral view of head region with palps and anterior to the left). **D.**

Treatment with mibefradil during neurulation phenocopies the *bug* phenotype. **E.** Treatment with nifedipine during neurulation stages causes an arrest in development. **F.** *Mibefradil treatments*. Dechorionated embryos at each developmental stage were subjected to control (water) or 1mM Mibefradil, washed after treatment, and then allowed to develop to swimming larvae stage. Percentage phenotype was calculated by counting the number of *bugeye*-like embryos over the total number of embryos treated. Error bars represent standard error of the mean from three independent experiments.

Figure 4.

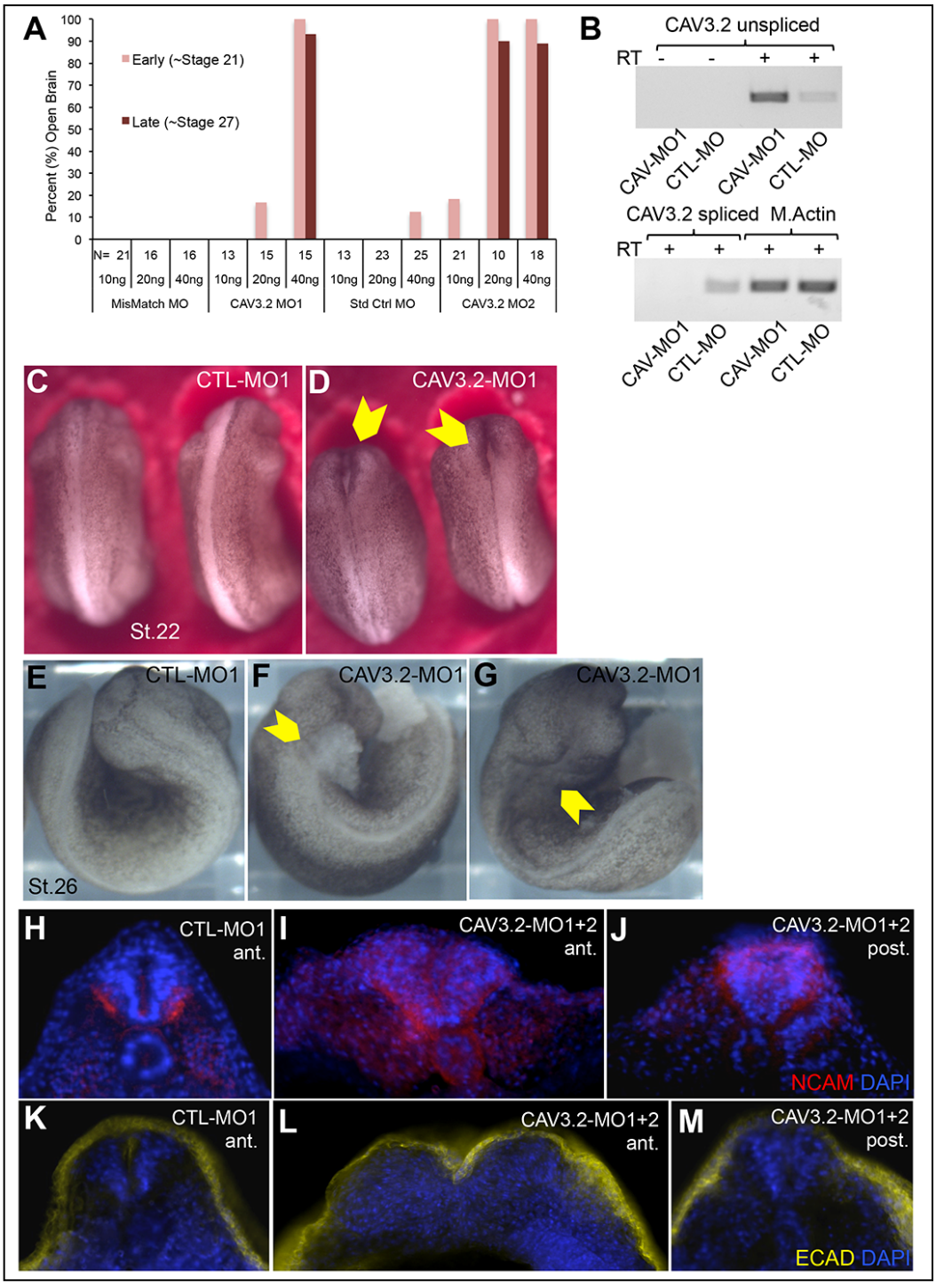

Figure 4. *X. laevis* CAV3.2 morpholino (MO) knockdown. **A.** Quantification of MO knockdown phenotype at stages 21 and 27. Two MOs targeting *X. laevis* CAV3.2 (CAV3.2-

MO1 and CAV3.2-MO2) and two control MOs [mismatch (CTL-MO1) and standard control (CTL-MO2); see Material and Methods)] were tested. The quantities of MO injected per embryo are indicated below the number (N) of embryos scored for each dose of MO. **B**. Disruption of CAV3.2 transcript splicing by CAV-MO1. RT-PCR was used to detect both the correct and expected splice-disrupted transcripts in cDNA samples from three pooled CTL-MO and three CAV-MO1 injected embryos. Muscle actin (M. Actin) RT-PCR was used to control for RNA load, and RT-minus controls are also shown. **C** and **D.** Early tailbud stage embryos (stage 22) injected at the one-cell stage with a CTL-MO1 (**C**), or a CAV3.2-MO1 (**D**). Yellow arrowheads in **B** indicate anterior open neural tube. **E-G**. Tailbud stage (stage 26) CTL-MO1 (**E**) and CAV3.2-MO1 (**F and G**) injected embryos. Anterior neural tube defects were observed in the CAV3.2-MO1 injections with either cellular matter erupting from the open neural tube (yellow arrowhead in **F**), or a with a malformed head and deep dimple in the hindbrain ((yellow arrowhead in **G**). **H-J**. NCAM staining (red) in anterior or posterior coronal sections of CTL-MO1 (**H**) and CAV3.2-MO1+2 (**I** and **J**) injected embryos. **K-M.** E-cadherin staining (yellow) in anterior and posterior coronal sections of CTL-MO1 (**K**) or CAV3.2-MO1+2 (**L** and **M**) injected embryos. MO injected embryos used for sections were stage matched at ~stage 24 based on somite development. All sections were also stained for nuclei (DAPI, blue).

Figure 5.

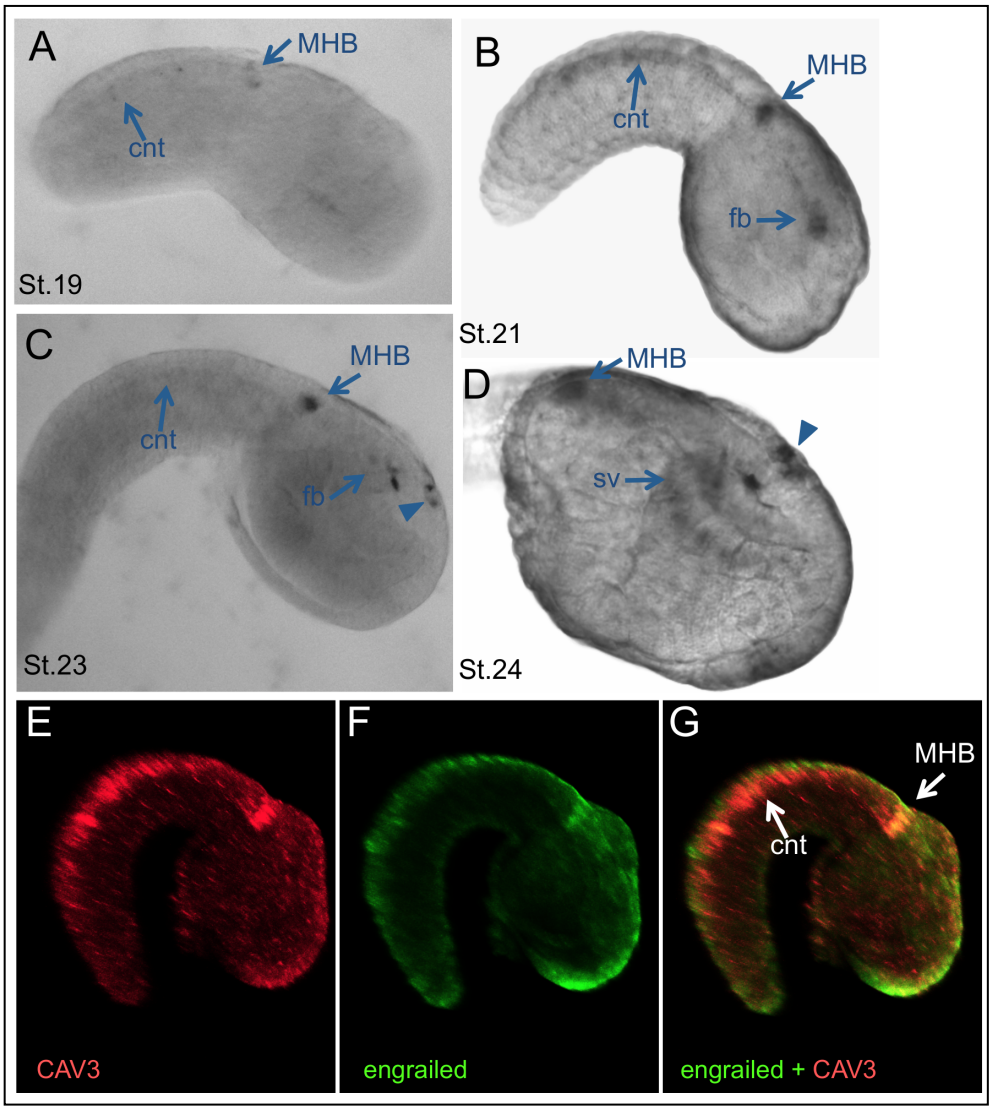

Figure 5. Expression of *C. savignyi* CAV3. **A-D.** In-situ hybridization of CAV3 expression in wild-type *C. savignyi* embryos. Expression is first detectable at early tailbud stage (**A**; stage 19) in the midbrain-hindbrain (MHB) region and faintly in the caudal nerve cord (cnt). This expression intensified by mid tailbud and new expression in the forebrain (fb) is observed (**B**; stage 21). By late tailbud (**C** and **D**; stage 23/24) new expression is seen in a cluster of cells in the epidermis (arrowheads) (sv=sensory vesicle). **E-G.** Double

fluorescent in situ for CAV3 and *engrailed* yields overlapping expression at the MHB (but not in the cnt). Embryos are stage 22.

Figure 6.

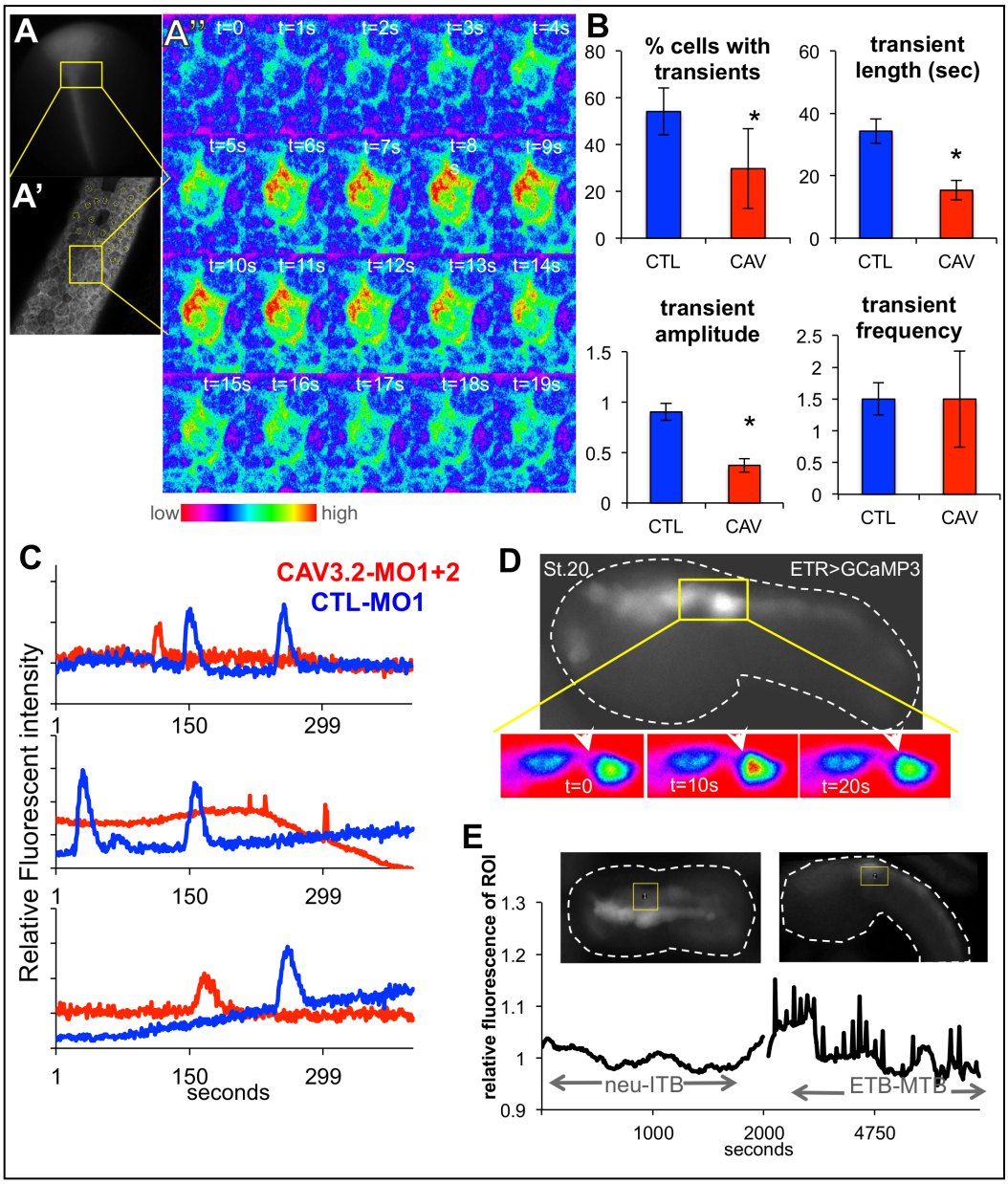

Figure 6. Calcium (Ca^{2+}) transients in the neural tubes of *C.savignyi* and *X. laevis*. **A-A''.** *Xenopus* embryo injected with GCaMP3 RNA shows Ca^{2+} transients during neurulation. Top left, a late neurula embryo expressing GCaMP3 in the closing neural tube (**A**). Low

magnification view of *X. laevis* embryo showing typical area recorded for Ca^{2+} transients (yellow box). Anterior is up . **A'**, High magnification of the Z plane of the *X. laevis* anterior neural plate that was imaged. **A''**. GCaMP fluorescence for a single cell in the neural plate undergoing a Ca^{2+} transient ([Ca^{2+}] indicated by color scale). **B**. CAV3.2 morpholino knockdown (CAV3.2-MO1, CAV) reduces the number of cells in the neural tube displaying Ca^{2+} transients, the length and amplitude of the transients, but not the frequency. The y-axis in the amplitude graph shows relative fluorescent intensity (see Materials and Methods). The frequency values are also described in Materials and Methods. Control embryos were injected with a non-specific MO (CTL-MO2, CTL). Data represent quantification of three embryos from three independent experiments and error bars represent standard error of the mean (*= $p<0.05$). **C.** Typical Ca^{2+} transients in CAV-MO knockdown and CTL-MO *X. laevis* neural tube cells. **D.** Ca^{2+} transients in *C. savignyi* embryos detected with GCaMP3 expressed from the pan-neural ETR1 promoter. Top panel shows one frame from a time-lapse movie. Lower panel is a close up of the midbrain hindbrain region (yellow box in top panel) showing a single Ca^{2+} transient with fluorescence intensity using the color scale from **A''**. **E.** Time-lapse of Ca^{2+} transients in the *C. savignyi* MHB region. Representative images from two time points (neurula and mid-tailbud) of an embryo expressing GCaMP3 with the MHB region of interest (ROI) outlined in yellow. Dashed white lines outline the embryo. Bottom panels show relative fluorescence intensity in the ROI over time. Neu-iTB = neurula to initial tailbud and ETB-MTB = early to mid tailbud.

Figure 7.

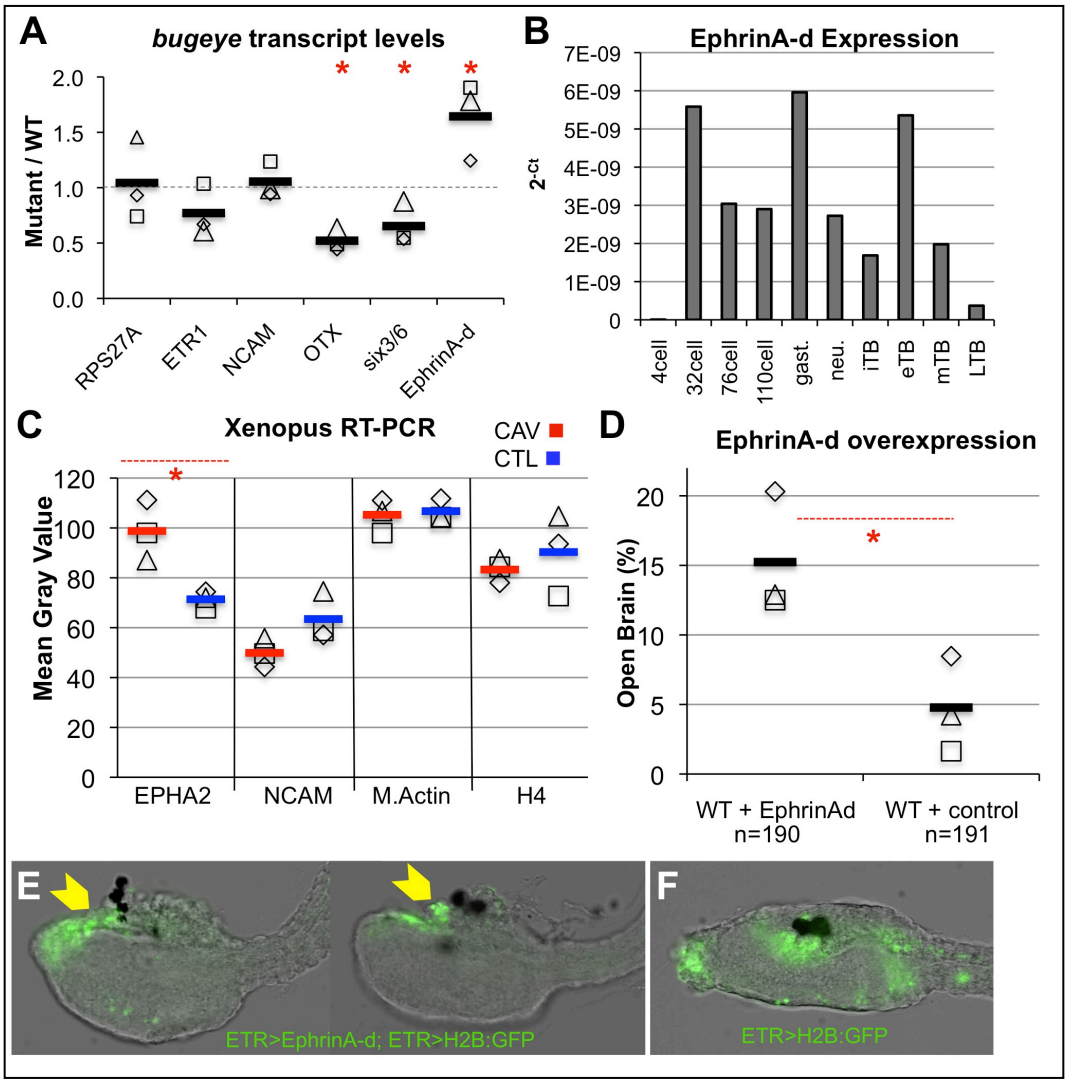

Figure 7. T-type Ca^{2+} channel regulation of EphrinA signaling components. **A**. qRT-PCR assay for expression of the neural genes *etr1, otx, six3/6, NCAM* and *ephrinA-d* in *bug* and wild type (WT) larvae. DDCT values were calculated by normalizing internally to the ubiquitously expressed gene *RPS27A* and then comparing to WT expression levels. The values for three independent biological repeats are indicated (open squares, etc) as well as the average of the three (black bar). Red asterisks indicates significant difference between bug mutants and WT for given transcript; $p \leq 0.05$, T-test. RPS27a values represent DCT

comparison to WT. **B.** *C. savignyi* EphrinA-d transcript levels quantified over developmental time. qRT-PCR results are represented as log2(X) changes in absolute cycle threshold values for each developmental time point sample. **C**. RT-PCR for expression of *EPHA2*, *NCAM, M.Actin and histone 4(H4)* in stage 24 *X. laevis* embryos injected with either CAV3.2 splice disrupting morpholinos (CAV-MO1+2, CAV), or a control MO (CTL-MO2, CTL). Solid color bars represent mean of gel densitometry readings from an assay of three embryos (open shapes). EPHA2 values are significantly different between CAV and CTL embryos (Red asterisks, p=0.025, Standard T-test). **D.** Percent of open brain phenotype observed in wild type embryos electroporated with either the EphrinA-d cDNA expression construct (WT+ EphrinAd), or H2B:GFP cDNA (WT+ control). Results from three independent trails are shown (open shapes), as well as the average of the three (black bars). Red asterisks indicates significance, p=0.0006, Fisher exact test. **E**. EphrinA-d overexpression driven by pan-neural ETR promoter in *C.intestinalis* embryos phenocopies *bug*. Yellow arrowheads indicate the open brain. Two representative embryos are shown. The co-electroporated plasmid ETR>H2B:GFP labels the nervous system. **F.** Control embryo expressing only ETR>H2B:GFP.

Figure 8.

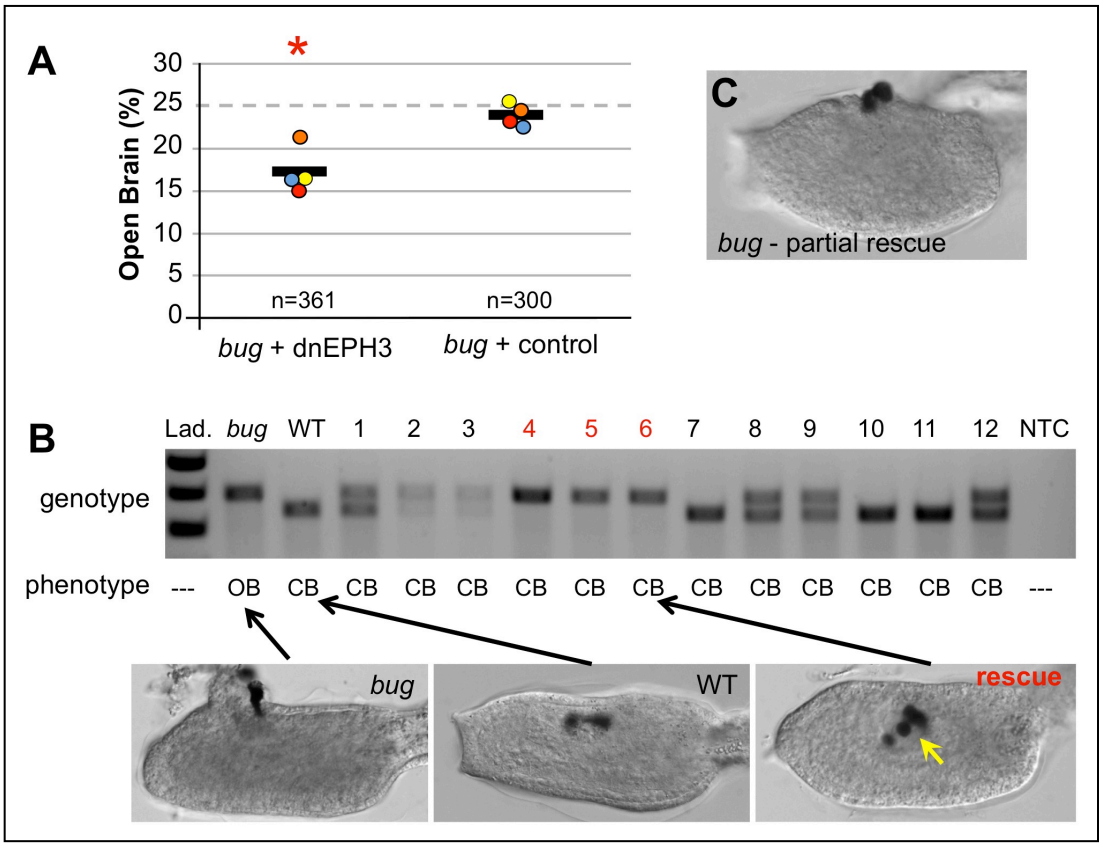

Figure 8. Rescue of *Ciona bugeye* (bug) embryos with dominant negative EPH3 (dnEPH3). **A.** Embryos from heterozygous *bug* parents were electroporated with either dnEPH3 driven by the pan-neural promoter ETR1, or an empty ETR1 vector (control). The fraction of embryos with the *bug* phenotype (open brain) was determined for each group. The circles represent the percent of embryos showing the *bug* phenotype from four independent trials, and the black line is the average of the four trials (*n* is the combined number scored from the four trials). Red asterisks indicate significant P-value of 0.002 using a chi-squared test of deviation from the expected open brain frequency of 25%. **B.** Single tadpoles electroporated with dnEPH3 (lanes 1-12) and scored as having closed brains (CB) were genotyped with primers that distinguished the insertion-containing *bug* allele (larger

PCR product) from the wild type allele. The *bug* and wild type (WT) lanes show the sizes the two alleles. Three of the twelve electroporated embryos (4-6, red) genotyped as homozygous for the *bug* allele despite having closed brains, and are considered as rescued. Representative images of wild type, *bug*, and rescued embryos are shown. **C.** Representative image of a partially rescued *bug* embryo**.**

Figure 9.

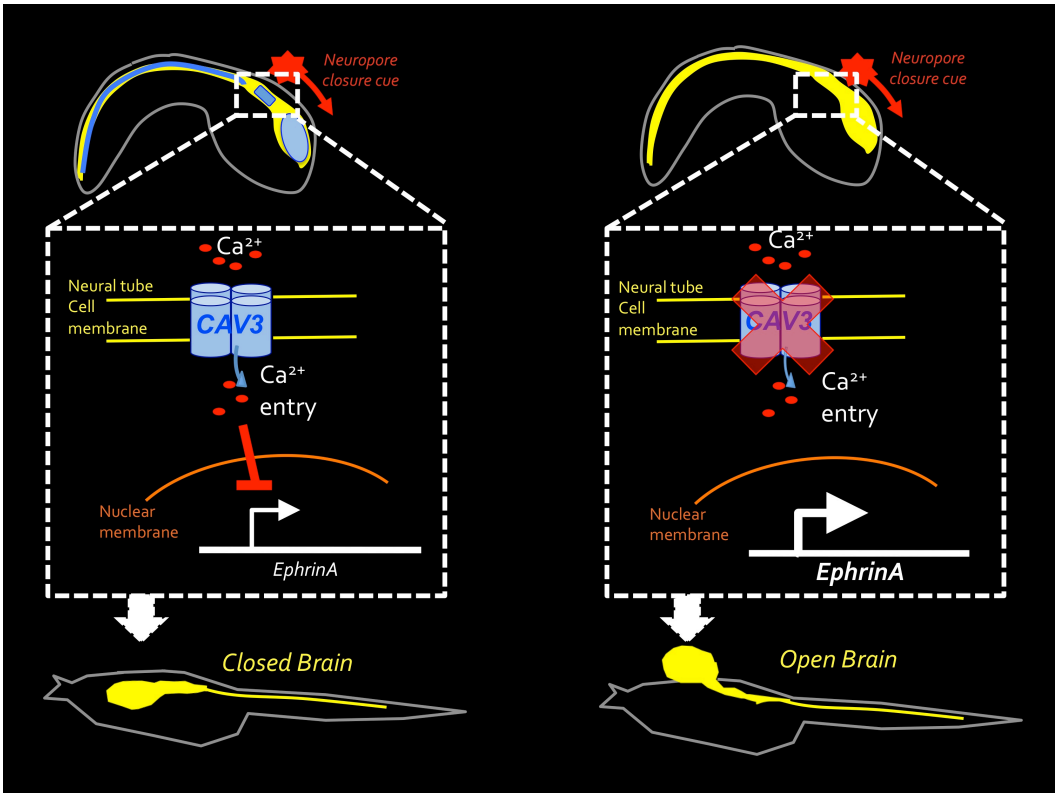

Figure 9. Proposed model of CAV3 function in neurulation. CAV3 expression (light blue) in the developing and closing neural tube (yellow) is necessary to seal the anterior neuropore. CAV3, a T-type calcium channel, most prominently expressed at the midbrain-hindbrain boundary, allows calcium entry into neural tube cells. A downstream effect of this is to create a repressive or inhibitory signal on transcript expression of the *EphrinA* gene

family. Down-regulated *EphrinA* expression at late neurulation stages allows for a closed and wild type brain.

Without correct CAV3 expression in the developing neural tube (right panel), the neuropore does not seal. Calcium entry into neural tube cells is misregulated with lack of CAV3 expression and subsequently permits overexpression of *EphrinA*. Increased *EphrinA* expression at late neurulation stages causes an open brain phenotype. Repressing the aberrant overexpression of *EphrinA* can rescue a CAV3 knockout, open-brain phenotype.

Supplemental Figure 1.

Supplemental Figure 1. Genotype of embryos from crossed *bugeye* heterozygous parents. W= wild type or closed brain phenotype. B= open brain or *bugeye* phenotype. Numbers indicate individuals assayed. Genotyping was done by PCR on genomic DNA with primers (*bugeye* genotype primer set, Supplemental Table 1) spanning the cis-regulatory insertion in *CAV3 bugeye*. 'Lad.' = base-pair ladder, 500, 400 and 300bp bands.

G. Tables

Table 1. Morpholino sequences

CAV3.2 spMO 1 (CAV-MO1)	TAACATCATCACTTACCATGCTCTC
CAV3.2 spMO 2 (CAV-MO2)	CCTCATACCTACATGAAAGAGGAGA
CAV3.2 mmMO 1 (CTL-MO2)	TAAgATgATgACTTACgATcCTCTC

Table 2. Primer sequences

X.laevis spMO detection intron F	ATGGTGCTCCAGGAAATGTT
X.laevis spMO detection exon F	TGGACACAATGTCAGCCTGT
X.laevis spMO detection exon R	TAAAACACCTGTTGCGCAGT
X.laevis M.Actin F	GCT GAC AGA ATG CAG AAG
X.laevis M.Actin R	TTG CTT GGA GGA GTG TGT
X.laevis NCAM F	GCAGCACAGTATTCATGGGG
X.laevis NCAM R	GCCTGAAATAGCTCTGATCCC
X.laevis EPHA2 F	AAATTCCGAGCTTGGTCGCT
X.laevis EPHA2 R	CCTTTGGCCCTGGCAACTAT
X.laevis Histone 4 F	GACGCTGTCACCTACACCGAG
X.laevis Histone 4 R	CGCCGAAGCCGTAGAGAGTG
C.intestinalis CAV3 ex3 MutDet F	TTGACCACTTTGTGTTTGCAT
C.intestinalis CAV3 ex49 MutDet R	AGAATCGGCCCTGACGTAAC
C.intestinalis CAV3 ex3 sgRNA	AGATGATGTTGGCAATGGGAGTGT
C.intestinalis CAV3 ex49 sgRNA	AGATGGTATGTCTAATGAACATGT
C.intestinalis FAT1 F	CCAAAACGATCCGGGACTTC
C.intestinalis FAT1 R	TTTTCAAAGTCCAGGCTGCC
C.savignyi EphrinA-d ORF +Kozak F	CAGAAAAA ATGTCATCTCAAATCA
C.savignyi EphrinA-d ORF R	TGCTGCAATAATCCCCCCAATGAGCCA
C.savignyi OTX ex4-6 F	CTGCACCTCCAGTTTACAGT
C.savignyi OTX ex4-6 R	TGTTGCTGTTTGTGCTTCCG
C.savignyi 636 F	CCATTGGGGCCAGTTGATAAG
C.savignyi 636 R	GCCCTGTCTCTTTGTCGTCT
C.savignyi NCAM ex12-13 F	TCCCCACCGAAGCTAATACC
C.savignyi NCAM ex12-13 R	GCTGGTTTCTCTTCCGCTTC
C.savignyi ETR1 F	ATGTTGGGGAAACGACAAAA
C.savignyi ETR1 R	ATCTGGAGGGGAACTGGATT
C.savignyi RPS27A F	CCACCTGATCAGCAGAGGTT
C.savignyi RPS27A R	TTATTCGCCCTCTGGTTTGA
C.savignyi CAV3 insitu F	TCCAGACCTGAGGAATGTCA
C.savignyi CAV3 insitu R	TCAGTTCGGACTGTGGTTCA
C.savignyi bugeye genotype F	TTCGCCAAACTTTGACTCCT
C.savignyi bugeye genotype R	CATGATGGGCTCGTCACC
C.savignyi Engrailed insitu F	TATAACCAAGGGGTGCAAGG
C.savignyi Engrailed insitu R	TTGAGCTAGCAACTGCATCG

REFERENCES

Abdul-Aziz, N.M., Turmaine, M., Greene, N.D., and Copp, A.J. (2009). EphrinA-EphA receptor interactions in mouse spinal neurulation: implications for neural fold fusion. The International journal of developmental biology *53*, 559-568.

Abdul-Wajid, S., Veeman, M.T., Chiba, S., Turner, T.L., and Smith, W.C. (2014). Exploiting the extraordinary genetic polymorphism of ciona for developmental genetics with whole genome sequencing. Genetics *197*, 49-59.

Andersen, E.C., Gerke, J.P., Shapiro, J.A., Crissman, J.R., Ghosh, R., Bloom, J.S., Felix, M.A., and Kruglyak, L. (2012). Chromosome-scale selective sweeps shape Caenorhabditis elegans genomic diversity. Nat Genet *44*, 285-290.

Arvanitis, D., and Davy, A. (2008). Eph/ephrin signaling: networks. Genes Dev *22*, 416-429.

Berger, J., Suzuki, T., Senti, K.A., Stubbs, J., Schaffner, G., and Dickson, B.J. (2001). Genetic mapping with SNP markers in Drosophila. Nat Genet *29*, 475-481.

Berthier, C., Monteil, A., Lory, P., and Strube, C. (2002). Alpha(1H) mRNA in single skeletal muscle fibres accounts for T-type calcium current transient expression during fetal development in mice. J Physiol *539*, 681-691.

Blackiston, D., Vandenberg, L.N., and Levin, M. (2010). High-throughput Xenopus laevis immunohistochemistry using agarose sections. Cold Spring Harb Protoc *2010*, pdb prot5532.

Blumenstiel, J.P., Noll, A.C., Griffiths, J.A., Perera, A.G., Walton, K.N., Gilliland, W.D., Hawley, R.S., and Staehling-Hampton, K. (2009). Identification of EMS-induced mutations in Drosophila melanogaster by whole-genome sequencing. Genetics *182*, 25-32.

Brandli, A.W., and Kirschner, M.W. (1995). Molecular cloning of tyrosine kinases in the early Xenopus embryo: identification of Eck-related genes expressed in cranial neural crest cells of the second (hyoid) arch. Dev Dyn *203*, 119-140.

Bronner-Fraser, M., Wolf, J.J., and Murray, B.A. (1992). Effects of antibodies against N-cadherin and N-CAM on the cranial neural crest and neural tube. Dev Biol *153*, 291-301.

Chen, C.C., Lamping, K.G., Nuno, D.W., Barresi, R., Prouty, S.J., Lavoie, J.L., Cribbs, L.L., England, S.K., Sigmund, C.D., Weiss, R.M., *et al.* (2003). Abnormal coronary function in mice deficient in alpha1H T-type Ca2+ channels. Science *302*, 1416-1418.

Cheng, R., Lim, J.E., Samocha, K.E., Sokoloff, G., Abney, M., Skol, A.D., and Palmer, A.A. (2010). Genome-wide association studies and the problem of relatedness among advanced intercross lines and other highly recombinant populations. Genetics *185*, 1033-1044.

Darby, A.C., and Hall, N. (2008). Fast forward genetics. Nat Biotechnol *26*, 1248-1249.

Davidson, L.A., and Keller, R.E. (1999). Neural tube closure in Xenopus laevis involves medial migration, directed protrusive activity, cell intercalation and convergent extension. Development *126*, 4547-4556.

Davis, M.W., Hammarlund, M., Harrach, T., Hullett, P., Olsen, S., and Jorgensen, E.M. (2005). Rapid single nucleotide polymorphism mapping in C. elegans. BMC Genomics *6*, 118.

Dehal, P., Satou, Y., Campbell, R.K., Chapman, J., Degnan, B., De Tomaso, A., Davidson, B., Di Gregorio, A., Gelpke, M., Goodstein, D.M.*, et al.* (2002). The draft genome of Ciona intestinalis: insights into chordate and vertebrate origins. Science *298*, 2157-2167.

Delsuc, F., Brinkmann, H., Chourrout, D., and Philippe, H. (2006). Tunicates and not cephalochordates are the closest living relatives of vertebrates. Nature *439*, 965-968.

Deschet, K., and Smith, W.C. (2004). Frimousse — a spontaneous ascidian mutant with anterior ectodermal fate transformation. Current Biology *14*, R408-R410.

Doitsidou, M., Poole, R.J., Sarin, S., Bigelow, H., and Hobert, O. (2010). C. elegans mutant identification with a one-step whole-genome-sequencing and SNP mapping strategy. PLoS One *5*, e15435.

Eom, D.S., Amarnath, S., Fogel, J.L., and Agarwala, S. (2011). Bone morphogenetic proteins regulate neural tube closure by interacting with the apicobasal polarity pathway. Development *138*, 3179-3188.

Ferron, L., Ruchon, Y., Renaud, J.F., and Capuano, V. (2011). T-type Ca(2)+ signalling regulates aldosterone-induced CREB activation and cell death through PP2A activation in neonatal cardiomyocytes. Cardiovasc Res *90*, 105-112.

Francois, A., Schuetter, N., Laffray, S., Sanguesa, J., Pizzoccaro, A., Dubel, S., Mantilleri, A., Nargeot, J., Noel, J., Wood, J.N.*, et al.* (2015). The Low-Threshold Calcium Channel Cav3.2 Determines Low-Threshold Mechanoreceptor Function. Cell reports.

Frischknecht, F., and Randall, A.D. (1998). Voltage- and ligand-gated ion channels in floor plate neuroepithelia of the rat. Neuroscience *85*, 1135-1149.

Ghosh, S., Marquardt, T., Thaler, J.P., Carter, N., Andrews, S.E., Pfaff, S.L., and Hunter, T. (2008). Instructive role of aPKCzeta subcellular localization in the assembly of adherens junctions in neural progenitors. Proc Natl Acad Sci U S A *105*, 335-340.

Gottmann, K., Dietzel, I.D., Lux, H.D., Huck, S., and Rohrer, H. (1988). Development of inward currents in chick sensory and autonomic neuronal precursor cells in culture. J Neurosci *8*, 3722-3732.

Greene, N.D., and Copp, A.J. (2014). Neural tube defects. Annual review of neuroscience *37*, 221-242.

Guryev, V., Koudijs, M.J., Berezikov, E., Johnson, S.L., Plasterk, R.H., van Eeden, F.J., and Cuppen, E. (2006). Genetic variation in the zebrafish. Genome Res *16*, 491-497.

Hackley, C., Mulholland, E., Kim, G.J., Newman-Smith, E., and Smith, W.C. (2013). A transiently expressed connexin is essential for anterior neural plate development in Ciona intestinalis. Development *140*, 147-155.

Haigo, S.L., Hildebrand, J.D., Harland, R.M., and Wallingford, J.B. (2003). Shroom induces apical constriction and is required for hingepoint formation during neural tube closure. Curr Biol *13*, 2125-2137.

Harrington, M.J., Hong, E., and Brewster, R. (2009). Comparative analysis of neurulation: first impressions do not count. Mol Reprod Dev *76*, 954-965.

Hashimoto, H., Robin, F.B., Sherrard, K.M., and Munro, E.M. (2015). Sequential contraction and exchange of apical junctions drives zippering and neural tube closure in a simple chordate. Dev Cell *32*, 241-255.

Haupaix, N., Abitua, P.B., Sirour, C., Yasuo, H., Levine, M., and Hudson, C. (2014). Ephrin-mediated restriction of ERK1/2 activity delimits the number of pigment cells in the Ciona CNS. Dev Biol *394*, 170-180.

Haupaix, N., Stolfi, A., Sirour, C., Picco, V., Levine, M., Christiaen, L., and Yasuo, H. (2013). p120RasGAP mediates ephrin/Eph-dependent attenuation of FGF/ERK signals during cell fate specification in ascidian embryos. Development *140*, 4347-4352.

Hildebrand, J.D. (2005). Shroom regulates epithelial cell shape via the apical positioning of an actomyosin network. J Cell Sci *118*, 5191-5203.

Hill, J.T., Demarest, B.L., Bisgrove, B.W., Gorsi, B., Su, Y.C., and Yost, H.J. (2013). MMAPPR: Mutation Mapping Analysis Pipeline for Pooled RNA-seq. Genome Res.

Hill, M.M., Broman, K.W., Stupka, E., Smith, W.C., Jiang, D., and Sidow, A. (2008). The C. savignyi genetic map and its integration with the reference sequence facilitates insights into chordate genome evolution. Genome Res *18*, 1369-1379.

Hillier, L.W., Marth, G.T., Quinlan, A.R., Dooling, D., Fewell, G., Barnett, D., Fox, P., Glasscock, J.I., Hickenbotham, M., Huang, W., *et al.* (2008). Whole-genome sequencing and variant discovery in C. elegans. Nat Methods *5*, 183-188.

Hobert, O. (2010). The impact of whole genome sequencing on model system genetics: get ready for the ride. Genetics *184*, 317-319.

Holmberg, J., Clarke, D.L., and Frisen, J. (2000). Regulation of repulsion versus adhesion by different splice forms of an Eph receptor. Nature *408*, 203-206.

Hotta, K., Mitsuhara, K., Takahashi, H., Inaba, K., Oka, K., Gojobori, T., and Ikeo, K. (2007). A web-based interactive developmental table for the ascidian Ciona intestinalis, including 3D real-image embryo reconstructions: I. From fertilized egg to hatching larva. Developmental dynamics : an official publication of the American Association of Anatomists *236*, 1790-1805.

Imai, K.S., Stolfi, A., Levine, M., and Satou, Y. (2009). Gene regulatory networks underlying the compartmentalization of the Ciona central nervous system. Development *136*, 285-293.

Jelier, R., Semple, J.I., Garcia-Verdugo, R., and Lehner, B. (2011). Predicting phenotypic variation in yeast from individual genome sequences. Nat Genet *43*, 1270-1274.

Ji, Y.J., Hwang, Y.S., Mood, K., Cho, H.J., Lee, H.S., Winterbottom, E., Cousin, H., and Daar, I.O. (2014). EphrinB2 affects apical constriction in Xenopus embryos and is regulated by ADAM10 and flotillin-1. Nat Commun *5*, 3516.

Jiang, D., Munro, E.M., and Smith, W.C. (2005a). Ascidian prickle regulates both mediolateral and anterior-posterior cell polarity of notochord cells. Curr Biol *15*, 79-85.

Jiang, D., Tresser, J.W., Horie, T., Tsuda, M., and Smith, W.C. (2005b). Pigmentation in the sensory organs of the ascidian larva is essential for normal behavior. The Journal of experimental biology *208*, 433-438.

Kano, S., Satoh, N., and Sordino, P. (2006). Primary genetic linkage maps of the ascidian, Ciona intestinalis. Zoolog Sci *23*, 31-39.

Kawakami, K., Imanaka, K., Itoh, M., and Taira, M. (2004). Excision of the Tol2 transposable element of the medaka fish Oryzias latipes in Xenopus laevis and Xenopus tropicalis. Gene *338*, 93-98.

Leclerc, C., Neant, I., and Moreau, M. (2012). The calcium: an early signal that initiates the formation of the nervous system during embryogenesis. Frontiers in molecular neuroscience *5*, 3.

Leffler, E.M., Bullaughey, K., Matute, D.R., Meyer, W.K., Segurel, L., Venkat, A., Andolfatto, P., and Przeworski, M. (2012). Revisiting an old riddle: what determines genetic diversity levels within species? PLoS Biol *10*, e1001388.

Lehner, B. (2013). Genotype to phenotype: lessons from model organisms for human genetics. Nat Rev Genet *14*, 168-178.

Leshchiner, I., Alexa, K., Kelsey, P., Adzhubei, I., Austin-Tse, C.A., Cooney, J.D., Anderson, H., King, M.J., Stottmann, R.W., Garnaas, M.K., *et al.* (2012). Mutation mapping and identification by whole-genome sequencing. Genome Res *22*, 1541-1548.

Lewis, B.B., Wester, M.R., Miller, L.E., Nagarkar, M.D., Johnson, M.B., and Saha, M.S. (2009). Cloning and characterization of voltage-gated calcium channel alpha1 subunits in Xenopus laevis during development. Developmental dynamics : an official publication of the American Association of Anatomists *238*, 2891-2902.

Li, H., and Durbin, R. (2009). Fast and accurate short read alignment with Burrows-Wheeler transform. Bioinformatics *25*, 1754-1760.

Li, H., Handsaker, B., Wysoker, A., Fennell, T., Ruan, J., Homer, N., Marth, G., Abecasis, G., and Durbin, R. (2009). The Sequence Alignment/Map format and SAMtools. Bioinformatics *25*, 2078-2079.

Lin, S.S., Tzeng, B.H., Lee, K.R., Smith, R.J., Campbell, K.P., and Chen, C.C. (2014). Cav3.2 T-type calcium channel is required for the NFAT-dependent Sox9 expression in tracheal cartilage. Proc Natl Acad Sci U S A *111*, E1990-1998.

Liti, G., and Louis, E.J. (2012). Advances in quantitative trait analysis in yeast. PLoS Genet *8*, e1002912.

Louhivuori, L.M., Louhivuori, V., Wigren, H.K., Hakala, E., Jansson, L.C., Nordstrom, T., Castren, M.L., and Akerman, K.E. (2013). Role of low voltage activated calcium channels in neuritogenesis and active migration of embryonic neural progenitor cells. Stem Cells Dev *22*, 1206-1219.

Luo, C., Tsementzi, D., Kyrpides, N., Read, T., and Konstantinidis, K.T. (2012). Direct comparisons of Illumina vs. Roche 454 sequencing technologies on the same microbial community DNA sample. PLoS One *7*, e30087.

Manni, L., Agnoletto, A., Zaniolo, G., and Burighel, P. (2005). Stomodeal and neurohypophysial placodes in Ciona intestinalis: insights into the origin of the pituitary gland. Journal of experimental zoology Part B, Molecular and developmental evolution *304*, 324-339.

Marchini, J., Howie, B., Myers, S., McVean, G., and Donnelly, P. (2007). A new multipoint method for genome-wide association studies by imputation of genotypes. Nat Genet *39*, 906-913.

Martin, R.L., Lee, J.H., Cribbs, L.L., Perez-Reyes, E., and Hanck, D.A. (2000). Mibefradil block of cloned T-type calcium channels. J Pharmacol Exp Ther *295*, 302-308.

Miller, A.C., Obholzer, N.D., Shah, A.N., Megason, S.G., and Moens, C.B. (2013). RNA-seq-based mapping and candidate identification of mutations from forward genetic screens. Genome Res *23*, 679-686.

Murdoch, J.N., Doudney, K., Paternotte, C., Copp, A.J., and Stanier, P. (2001). Severe neural tube defects in the loop-tail mouse result from mutation of Lpp1, a novel gene involved in floor plate specification. Hum Mol Genet *10*, 2593-2601.

Nelson, M.T., Todorovic, S.M., and Perez-Reyes, E. (2006). The role of T-type calcium channels in epilepsy and pain. Curr Pharm Des *12*, 2189-2197.

Nishida, H. (1987). Cell lineage analysis in ascidian embryos by intracellular injection of a tracer enzyme. III. Up to the tissue restricted stage. Dev Biol *121*, 526-541.

O'Rourke, S.M., Yochem, J., Connolly, A.A., Price, M.H., Carter, L., Lowry, J.B., Turnbull, D.W., Kamps-Hughes, N., Stiffler, N., Miller, M.R., *et al.* (2011). Rapid mapping and identification of mutations in Caenorhabditis elegans by restriction site-associated DNA mapping and genomic interval pull-down sequencing. Genetics *189*, 767-778.

Obholzer, N., Swinburne, I.A., Schwab, E., Nechiporuk, A.V., Nicolson, T., and Megason, S.G. (2012). Rapid positional cloning of zebrafish mutations by linkage and homozygosity mapping using whole-genome sequencing. Development *139*, 4280-4290.

Okamura, Y., Nishino, A., Murata, Y., Nakajo, K., Iwasaki, H., Ohtsuka, Y., Tanaka-Kunishima, M., Takahashi, N., Hara, Y., Yoshida, T., *et al.* (2005a). Comprehensive analysis of the ascidian genome reveals novel insights into the molecular evolution of ion channel genes. Physiol Genomics *22*, 269-282.

Okamura, Y., Nishino, A., Murata, Y., Nakajo, K., Iwasaki, H., Ohtsuka, Y., Tanaka-Kunishima, M., Takahashi, N., Hara, Y., Yoshida, T., *et al.* (2005b). Comprehensive analysis of the ascidian genome reveals novel insights into the molecular evolution of ion channel genes. Physiol Genomics *22*, 269-282.

Olinski, R.P., Dahlberg, C., Thorndyke, M., and Hallbook, F. (2006). Three insulin-relaxin-like genes in Ciona intestinalis. Peptides *27*, 2535-2546.

Park, E.C., Cho, G.S., Kim, G.H., Choi, S.C., and Han, J.K. (2011). The involvement of Eph-Ephrin signaling in tissue separation and convergence during Xenopus gastrulation movements. Dev Biol *350*, 441-450.

Passamaneck, Y.J., and Di Gregorio, A. (2005). Ciona intestinalis: chordate development made simple. Dev Dyn *233*, 1-19.

Perez-Reyes, E. (2003). Molecular physiology of low-voltage-activated t-type calcium channels. Physiological reviews *83*, 117-161.

Perez-Reyes, E., and Lory, P. (2006). Molecular biology of T-type calcium channels. CNS Neurol Disord Drug Targets *5*, 605-609.

Picco, V., Hudson, C., and Yasuo, H. (2007). Ephrin-Eph signalling drives the asymmetric division of notochord/neural precursors in Ciona embryos. Development *134*, 1491-1497.

Pyrgaki, C., Liu, A., and Niswander, L. (2011). Grainyhead-like 2 regulates neural tube closure and adhesion molecule expression during neural fold fusion. Dev Biol *353*, 38-49.

Raible, F., and Brand, M. (2004). Divide et Impera--the midbrain-hindbrain boundary and its organizer. Trends in neurosciences *27*, 727-734.

Ran, F.A., Hsu, P.D., Wright, J., Agarwala, V., Scott, D.A., and Zhang, F. (2013). Genome engineering using the CRISPR-Cas9 system. Nature protocols *8*, 2281-2308.

Robinson, J.T., Thorvaldsdottir, H., Winckler, W., Guttman, M., Lander, E.S., Getz, G., and Mesirov, J.P. (2011). Integrative genomics viewer. Nat Biotechnol *29*, 24-26.

Rosenberg, S.S., and Spitzer, N.C. (2011). Calcium signaling in neuronal development. Cold Spring Harb Perspect Biol *3*, a004259.

Roure, A., Rothbacher, U., Robin, F., Kalmar, E., Ferone, G., Lamy, C., Missero, C., Mueller, F., and Lemaire, P. (2007). A multicassette Gateway vector set for high throughput and comparative analyses in ciona and vertebrate embryos. PLoS One *2*, e916.

Satoh, N. (1994). Developmental biology of ascidians (Cambridge England ; New York, Cambridge University Press).

Satou, Y., Shin-i, T., Kohara, Y., Satoh, N., and Chiba, S. (2012). A genomic overview of short genetic variations in a basal chordate, Ciona intestinalis. BMC Genomics *13*, 208.

Schneeberger, K., Ossowski, S., Lanz, C., Juul, T., Petersen, A.H., Nielsen, K.L., Jorgensen, J.E., Weigel, D., and Andersen, S.U. (2009). SHOREmap: simultaneous mapping and mutation identification by deep sequencing. Nat Methods *6*, 550-551.

Scott, L., LaFoe, D., and Weil, C.F. (1996). Adjacent sequences influence DNA repair accompanying transposon excision in maize. Genetics *142*, 237-246.

Shoguchi, E., Kawashima, T., Satou, Y., Hamaguchi, M., Sin, I.T., Kohara, Y., Putnam, N., Rokhsar, D.S., and Satoh, N. (2006). Chromosomal mapping of 170 BAC clones in the ascidian Ciona intestinalis. Genome Res *16*, 297-303.

Silva, N., and Smith, W.C. (2008). Inverse correlation of population similarity and introduction date for invasive ascidians. PLoS One *3*, e2552.

Sive, H.L., Grainger, R.M., and Harland, R.M. (2000). Early development of Xenopus laevis : a laboratory manual (Cold Spring Harbor, N.Y., Cold Spring Harbor Laboratory Press).

Sive, H.L., Grainger, R.M., and Harland, R.M. (2007). Inducing Ovulation in Xenopus laevis. CSH Protoc *2007*, pdb prot4734.

Small, K.S., Brudno, M., Hill, M.M., and Sidow, A. (2007a). Extreme genomic variation in a natural population. Proc Natl Acad Sci U S A *104*, 5698-5703.

Small, K.S., Brudno, M., Hill, M.M., and Sidow, A. (2007b). A haplome alignment and reference sequence of the highly polymorphic Ciona savignyi genome. Genome Biol *8*, R41.

Smith, A., Robinson, V., Patel, K., and Wilkinson, D.G. (1997). The EphA4 and EphB1 receptor tyrosine kinases and ephrin-B2 ligand regulate targeted migration of branchial neural crest cells. Curr Biol *7*, 561-570.

Solecki, D.J., Govek, E.E., Tomoda, T., and Hatten, M.E. (2006). Neuronal polarity in CNS development. Genes Dev *20*, 2639-2647.

Stolfi, A., Gandhi, S., Salek, F., and Christiaen, L. (2014). Tissue-specific genome editing in Ciona embryos by CRISPR/Cas9. Development *141*, 4115-4120.

Stolfi, A., Wagner, E., Taliaferro, J.M., Chou, S., and Levine, M. (2011). Neural tube patterning by Ephrin, FGF and Notch signaling relays. Development *138*, 5429-5439.

Takamura, K., Oka, N., Akagi, A., Okamoto, K., Okada, T., Fukuoka, T., Hogaki, A., Naito, D., Oobayashi, Y., and Satoh, N. (2001). EST analysis of genes that are expressed in the neural complex of Ciona intestinalis adults. Zoolog Sci *18*, 1231-1236.

Thorvaldsdottir, H., Robinson, J.T., and Mesirov, J.P. (2013). Integrative Genomics Viewer (IGV): high-performance genomics data visualization and exploration. Brief Bioinform *14*, 178-192.

Tian, L., Hires, S.A., Mao, T., Huber, D., Chiappe, M.E., Chalasani, S.H., Petreanu, L., Akerboom, J., McKinney, S.A., Schreiter, E.R.*, et al.* (2009). Imaging neural activity in worms, flies and mice with improved GCaMP calcium indicators. Nat Methods *6*, 875-881.

Tresser, J., Chiba, S., Veeman, M., El-Nachef, D., Newman-Smith, E., Horie, T., Tsuda, M., and Smith, W.C. (2010). doublesex/mab3 related-1 (dmrt1) is essential for development of anterior neural plate derivatives in Ciona. Development *137*, 2197-2203.

Tsuda, M., Kusakabe, T., Iwamoto, H., Horie, T., Nakashima, Y., Nakagawa, M., and Okunou, K. (2003). Origin of the vertebrate visual cycle: II. Visual cycle proteins are localized in whole brain including photoreceptor cells of a primitive chordate. Vision Res *43*, 3045-3053.

Veeman, M.T., Chiba, S., and Smith, W.C. (2011a). Ciona genetics. Methods Mol Biol *770*, 401-422.

Veeman, M.T., Chiba, S., and Smith, W.C. (2011b). Ciona genetics. Methods Mol Biol *770*, 401-422.

Veeman, M.T., Nakatani, Y., Hendrickson, C., Ericson, V., Lin, C., and Smith, W.C. (2008). Chongmague reveals an essential role for laminin-mediated boundary formation in chordate convergence and extension movements. Development *135*, 33-41.

Veeman, M.T., Newman-Smith, E., El-Nachef, D., and Smith, W.C. (2010). The ascidian mouth opening is derived from the anterior neuropore: reassessing the mouth/neural tube relationship in chordate evolution. Dev Biol *344*, 138-149.

Vinson, J.P., Jaffe, D.B., O'Neill, K., Karlsson, E.K., Stange-Thomann, N., Anderson, S., Mesirov, J.P., Satoh, N., Satou, Y., Nusbaum, C.*, et al.* (2005). Assembly of polymorphic genomes: algorithms and application to Ciona savignyi. Genome Res *15*, 1127-1135.

Wallingford, J.B. (2005). Neural tube closure and neural tube defects: studies in animal models reveal known knowns and known unknowns. Am J Med Genet C Semin Med Genet *135C*, 59-68.

Wallingford, J.B., and Harland, R.M. (2001). Xenopus Dishevelled signaling regulates both neural and mesodermal convergent extension: parallel forces elongating the body axis. Development *128*, 2581-2592.

Wallingford, J.B., Niswander, L.A., Shaw, G.M., and Finnell, R.H. (2013). The continuing challenge of understanding, preventing, and treating neural tube defects. Science *339*, 1222002.

Watterson, G.A. (1975). On the number of segregating sites in genetical models without recombination. Theor Popul Biol *7*, 256-276.

Watterson, G.A. (1978). The homozygosity test of neutrality. Genetics *88*, 405-417.

Ybot-Gonzalez, P., and Copp, A.J. (1999). Bending of the neural plate during mouse spinal neurulation is independent of actin microfilaments. Dev Dyn *215*, 273-283.

Zohn, I.E., and Sarkar, A.A. (2012). Does the cranial mesenchyme contribute to neural fold elevation during neurulation? Birth Defects Res A Clin Mol Teratol *94*, 841-848.